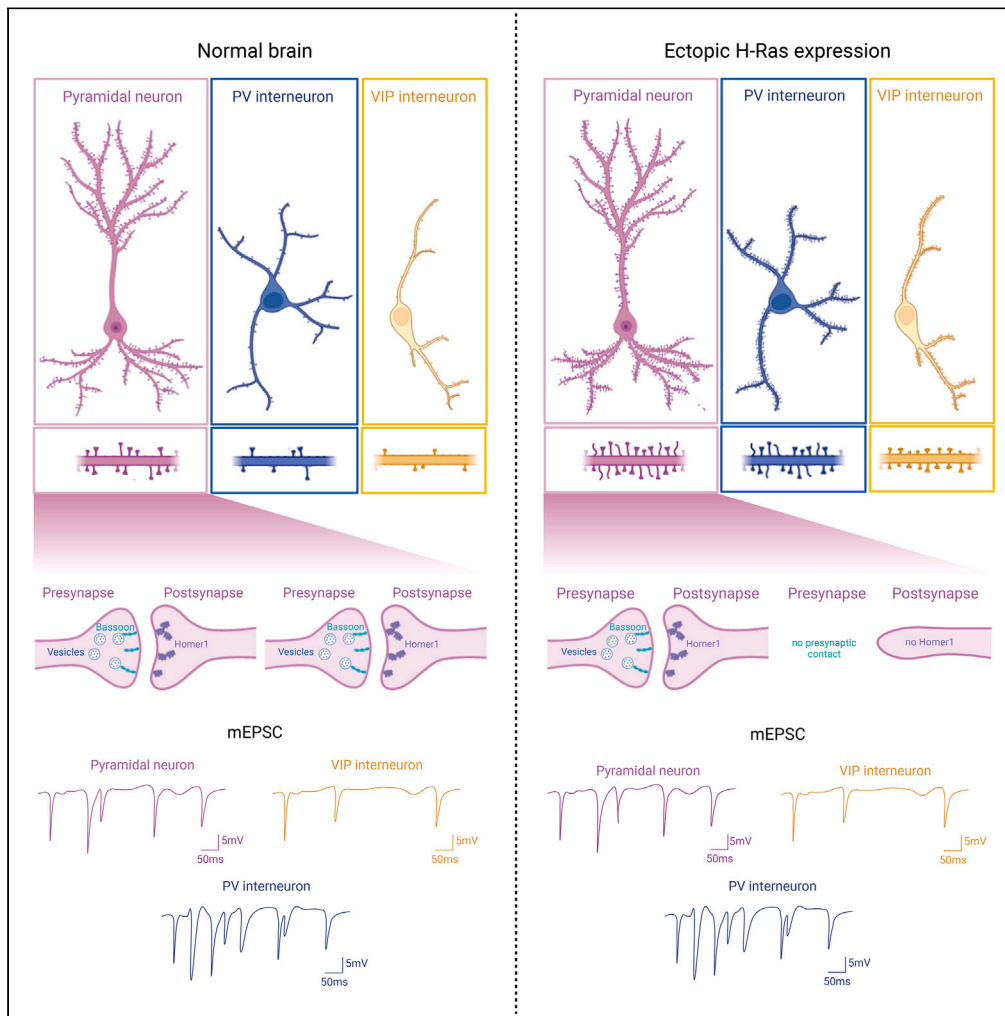**Article**

H-Ras induces exuberant *de novo* dendritic protrusion growth in mature neurons regardless of cell type

Sarah Krüssel,
Ishana Deb,
Seungkyu Son, ...,
Hey-Kyoung Lee,
Won Do Heo,
Hyung-Bae Kwon

hkwon29@jhmi.edu

Highlights

H-Ras expression enhances dendritic protrusion numbers in PyNs, PV, and VIP INs

Increase is carried by filopodia in PyNs, dendritic spines in VIP INs, and both in PV INs

Newly formed dendritic protrusions seem to be functionally silent

Article

H-Ras induces exuberant *de novo* dendritic protrusion growth in mature neurons regardless of cell type

Sarah Krüssel,[1] Ishana Deb,[1] Seungkyu Son,[2] Gabrielle Ewall,[3] Minhyeok Chang,[1] Hey-Kyoung Lee,[3,4] Won Do Heo,[2] and Hyung-Bae Kwon[1,5,*]

SUMMARY

Dendritic protrusions, mainly spines and filopodia, correlate with excitatory synapses in pyramidal neurons (PyNs), but this relationship may not apply universally. We found that ectopic H-Ras expression increased protrusions across various cortical cell types, including layer 2/3 PyNs, parvalbumin (PV)-, and vasoactive intestinal peptide (VIP)-positive interneurons (INs) in the primary motor cortex. The probability of detecting protrusions correlated with local H-Ras activity, indicating its role in protrusion formation. H-Ras overexpression led to high turnover rates by adding protrusions. Two-photon photolysis of glutamate induced *de novo* spine formation in mature H-Ras expressing neurons, suggesting H-Ras's effect is not limited to early development. In PyNs and PV-INs, but not VIP-INs, spine neck lengths shifted to filopodia-like phenotypes. H-Ras primarily induced filopodia in PyNs and spines in PV- and VIP-INs. Increased protrusions in H-Ras-transfected PyNs lacked key excitatory synaptic proteins and did not affect miniature excitatory postsynaptic currents (mEPSCs), suggesting multifaceted roles beyond excitatory synapses.

INTRODUCTION

Dendritic spines are small membrane protrusions stemming from the dendrites of neurons. They serve as a structural compartment for the efficient transfer of information from one neuron to another. During learning or normal development, these synapses undergo reorganization to establish functionally specific neural circuits.[1–9] Since most excitatory synapses contain these dendritic spines in the mammalian brain, examination of dendritic spine dynamics has been regarded as an anatomical proxy for changes in neural connectivity. Because of the strong association between dendritic spines and functional synapses, many molecules involved in spine number changes were identified as cell adhesion molecules.[10–13]

Dendritic spines have also been reported to develop in the absence of presynaptic terminals. Filopodia, as dendritic spine precursors, are abundant during development. These highly dynamic structures, characterized by their long spine necks and the lack of a spine head, are believed to serve as excellent explorers, actively seeking out axonal boutons, establishing initial connections, and ultimately forming spine-like protrusions.[14,15] Recent studies challenge the notion that filopodia are rare in adulthood, suggesting that conventional microscopy techniques may underestimate their prevalence.[16] Hence, filopodia's role in spine formation may extend beyond the developmental stage. However, the precise mechanism and prevalence of filopodia precursors remains uncertain. Focal, repetitive release of glutamate near the dendrite by two-photon photolysis was able to generate *de novo* dendritic spines and filopodia in layer 2/3 pyramidal neurons (PyNs) of the somatosensory cortex, but these newly formed protrusions often bypassed the filopodia stage and directly transitioned into mushroom spines.[17,18] The glutamate-induced spinogenesis was not just limited to the somatosensory cortex but was also found in other cortical brain areas, such as motor cortex and prefrontal cortex.[19,20] Hippocampal PyNs and medium spiny neurons in the striatum also showed a similar process of spine formation.[21,22] These data indicate that glutamate itself is a sufficient trigger for spinogenesis. Photolytic induction of spine formation was not uniformly successful, even among sites on the same dendritic branch with similar levels of glutamate receptor density.[17] This observation suggests that what determines successful spinogenesis may not be the amount of glutamate or the postsynaptic receptor density. Furthermore, γ-aminobutyric acid (GABA), an inhibitory neurotransmitter, also produced dendritic spines,[18] indicating that the determining factor for spine formation is not the identity of neurotransmitter but is rather a postsynaptic factor.

[1]Solomon H. Snyder Department of Neuroscience, Johns Hopkins University School of Medicine, Baltimore, MD 21205, USA
[2]Department of Biological Sciences, Korea Advanced Institute of Science and Technology (KAIST), Daejeon 34141, Republic of Korea
[3]Solomon H. Snyder Department of Neuroscience, Zanvyl-Krieger Mind/Brain Institute, Johns Hopkins School of Medicine, Baltimore, MD, USA
[4]Kavli Neuroscience Discovery Institute, Johns Hopkins University, Baltimore, MD, USA
[5]Lead contact
*Correspondence: hkwon29@jhmi.edu
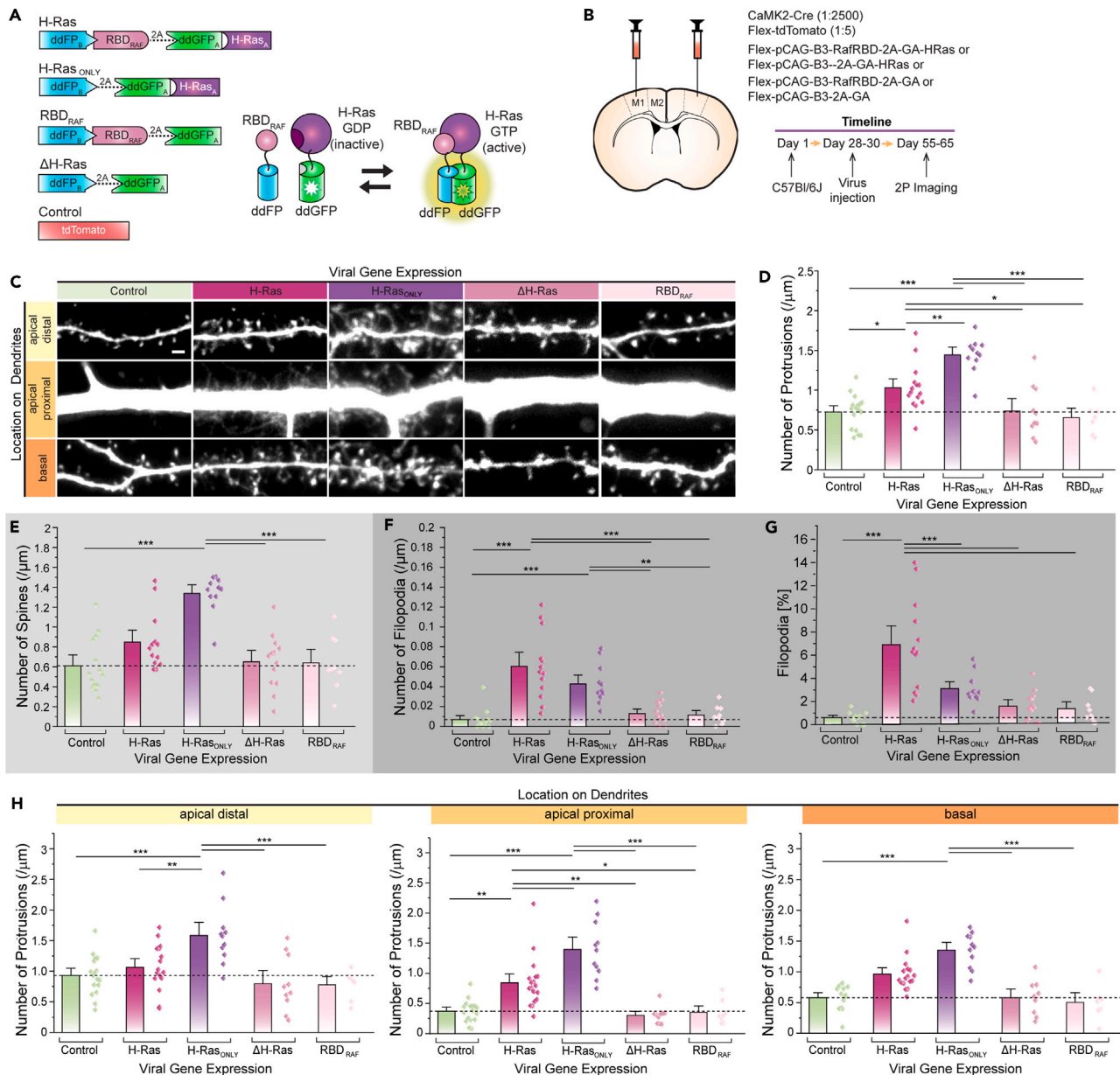https://doi.org/10.1016/j.isci.2024.110535

Figure 1. H-Ras increases protrusion number in cortical pyramidal neurons

(A) Left: schematic depiction of H-Ras sensor constructs and its controls (H-Ras$_{ONLY}$, RBD$_{RAF}$, ΔH-Ras, and Control). Right: schematic of the mode of action of ddFP-based H-Ras sensor.

(B) Virus injection scheme and experimental timeline.

(C) Two-photon microscopy images showing representative dendrites (apical distal, apical proximal, and basal) of pyramidal neurons expressing Flex-tdTomato in the primary motor cortex of a typical acute brain slice made from C57Bl6 mice at ∼ P60 injected 4-week prior with CaMKII-Cre, Flex-tdTomato, and either Flex-pCAG-B3-RafRBD-2A-GA-HRas (H-Ras), Flex-pCAG-B3-2A-GA-HRas (H-Ras$_{ONLY}$), Flex-pCAG-B3-RafRBD-2A-GA (RBD$_{RAF}$) or Flex-pCAG-B3-2A-GA (ΔH-Ras). Scale bar, 2 μm.

(D) A summary graph showing the protrusion density. Dots represent average protrusion number from each neuron (dots) and bars indicate mean ± SEM, respectively for each condition (control: 0.7259 ± 0.05162, n = 17; H-Ras:1.0316 ± 0.0743, n = 15; H-Ras$_{ONLY}$: 1.4443 ± 0.0657, n = 11; ΔH-Ras: 0.73881 ± 0.10413, n = 10; and RBD$_{RAF}$: 0.6554 ± 0.07848, n = 7). The dotted line represents the average protrusion density of the tdTomato only control. $*p < 0.05$ (one-way ANOVA, post-hoc: Tukey test).

(E–G) Light shaded box shows graphs related to dendritic spines (E) and dark shaded box shows data related to filopodia (F and G). Separation of protrusions into spines (E) and filopodia (F) showing their density. Dots represent average numbers from each neuron and bars indicate mean ± SEM, respectively, for each condition; (E) control: 0.6096 ± 0.739, n = 14; H-Ras: 0.8479 ± n = 13; H-Ras$_{ONLY}$: 1.338 ± 0.0577, n = 11; ΔH-Ras: 0.6507 ± 0.0764, n = 13; RBD$_{RAF}$: 0.6398 ± 0.0902, n = 9; (F) Control: 0.0068 ± 0.0027, n = 14; H-Ras: 0.0605 ± 0.0094, n = 13; H-Ras$_{ONLY}$: 0.0427 ± 0.006, n = 11; ΔH-Ras: 0.0106 ± 0.003,

Figure 1. Continued

n = 13; RBD$_{RAF}$: 0.0115 ± 0.0031, n = 9. The H-Ras effect seems to be mostly due to an increase in filopodia number, however, H-Ras$_{ONLY}$ showed an increase in both filopodia and spine number. *$p < 0.05$, ***$p < 0.001$ (one-way ANOVA, post-hoc: Tukey test).

(G) Percentage of filopodia of individual neurons (dots) and the mean ± SEM filopodia percentage (control: 0.6059 ± 0.1377, n = 12; H-Ras: 6.9017 ± 1.0834, n = 13; H-Ras$_{ONLY}$: 3.067 ± 0.3917, n = 11; ΔH-Ras: 1.4622 ± 0.3541, n = 14, and RBD$_{RAF}$: 1.2259 ± 0.3908, n = 9). Pyramidal neurons expressing ectopic H-Ras have higher percentages of filopodia. ***$p < 0.001$ (one-way ANOVA, post-hoc: Tukey test).

(H) Separation of protrusion density analysis into the three dendritic locations: apical distal, apical proximal and basal. Apical distal: control (0.931 ± 0.0776), H-Ras (1.06549 ± 0.09451), H-Ras$_{ONLY}$: (1.58348 ± 0.1445), ΔH-Ras (0.79241 ± 0.14282), and RBD$_{RAF}$ (0.77855 ± 0.09053); apical proximal: control (0.37316 ± 0.0448), H-Ras (0.84397 ± 0.0987), H-Ras$_{ONLY}$ (1.39342 ± 0.13986), ΔH-Ras (0.30431 ± 0.04335), and RBD$_{RAF}$ (0.35444 ± 0.06879); basal: control (0.5743 ± 0.05578), H-Ras (0.95856 ± 0.06823), H-Ras$_{ONLY}$: (1.3534 ± 0.08495), ΔH-Ras (0.58031 ± 0.09471), and RBD$_{RAF}$ (0.5017 ± 0.107). control: n = 17; H-Ras: n = 15; H-Ras$_{ONLY}$: n = 11, ΔH-Ras: n = 10; RBD$_{RAF}$: n = 7. *$p < 0.05$, **$p < 0.01$, ***$p < 0.001$ (two-way ANOVA, Post-hoc: Tukey test).

See also Figures S1, S2, and S3.

In further support of this theory, Sigler et al. found that dendritic spines and filopodia in a mouse mutant lacking Munc13-1/Munc13-2 (M13 double knockout [M13 DKO]) formed normally despite complete abolition of both glutamate and GABA release.[23] Another genetic manipulation that abolished vesicular glutamate release also showed normal spine density.[24] Whether these activity-independently formed spines are able to make functional synapses is still unknown, but their morphology was not different from functional spines and their ultrastructure showed normal contact to the presynaptic boutons.[23–25] Evidence that glutamatergic neurotransmission is unnecessary for dendritic spine formation was also shown by selective deletion of ionotropic glutamatergic receptors in hippocampal CA1 PyNs.[26] Thus, it seems apparent that dendritic spines are induced in the absence of neurotransmitters or receptor activation.

Despite these findings, what remains unclear is which molecules directly mediate dendritic spine and filopodia formation and whether these spines and filopodia always become functional synapses. In adulthood, learning induces new filopodia and ultimately spines not randomly but in a clustered manner, with new filopodia and spines being added in close proximity to preexisting stable spines involved in the task.[1,27–31] Preexisting spines exhibit signs of recent structural plasticity suggesting that signaling molecules spread from the stimulated spine to nearby dendritic segments priming the area for *de novo* filopodia and spine formation.[17,27,28] One molecule that could play such a role is the small GTPase H-Ras, which is known to be activated by after long-term potentiation (LTP), remain active for up to 5 min and travel up to ∼10 μm away from the induction site.[27,32,33] Furthermore, inhibition of H-Ras downstream signaling molecule, mitogen-activated kinase (MAPK) kinase 1/2 (MEK1/2), has been shown to reduce the success of photolytic induction of spine formation.[17] Additionally, "priming" of a pre-existing spine via glutamate photolysis, followed by a "test" subthreshold stimulus on a nearby dendritic shaft enhanced the success rate of spinogenesis in a MEK1/2-dependent manner.[17] Interestingly, mutations resulting in constitutive activation of Ras and exposure to brain-derived neurotrophic factor (BDNF), an upstream effector of H-Ras, were observed to increase the number of filopodia, while dendritic spines were reduced,[34] suggesting that H-Ras is selectively involved in filopodia formation.

Here, we found that H-Ras overexpression increased filopodia numbers in excitatory PyNs, and predominately dendritic spine numbers in parvalbumin (PV)- and vasoactive intestinal peptide (VIP)-positive interneurons (INs). Interestingly, the most pronounced change in density was observed in the two different types of INs that normally do not express a high density of dendritic spines.[35–43] When investigating protrusion dynamics in PyNs, H-Ras did not affect protrusion elimination rates but increased the probability of new dendritic protrusion formation in the presence and absence of external activity. These findings imply that H-Ras functions as a spinogenic molecule that produces dendritic protrusions independent of cell type. We uncovered that the increased number of protrusions was not coupled with functional connectivity changes in PyN, PV INs, or VIP INs. These data pave the way for further exploration of the nature of non-functional filopodia and dendritic spines.

RESULTS

H-Ras increases filopodia number in pyramidal cells

We investigated the role of H-Ras on the spinogenesis of mature PyNs in layer 2/3 of the neocortex. Recently developed intensiometric small GTPase biosensors allow for simultaneous overexpression and visualization of small GTPase activity patterns.[44] In this study, we used the intensiometric small GTPase biosensor to overexpress H-Ras, specifically, and detect its activity. In its active state, H-Ras interacts with its effector domain RAF initiating downstream signaling.[45] This feature of heterodimerization is here coupled with the heterodimerization of two quenched fluorescent protein-derived monomers of ddFP, copy A and copy B, which produce bright green fluorescence when reunited (Figure 1A). Copy A was bound to H-Ras and copy B to the Ras-binding domain of RAF (RBD$_{RAF}$) sensing H-Ras activity upon H-Ras/RBD$_{RAF}$ binding. As controls, we created three biosensor versions: one devoid of its H-Ras component (from here on referred to as "RBD$_{RAF}$"), one devoid of its RBD$_{RAF}$ component (from here on referred to as "H-Ras$_{ONLY}$"), and one biosensor version containing only the biosensor backbone without any signaling proteins (from here on referred to as "ΔH-Ras") (Figure 1A).

For morphometric analysis, two aspects are of importance for optimal image and analysis quality: (1) expression of a cell marker protein and (2) a high signal-to-noise ratio. In this study, we used a red fluorescence protein as a cell marker and injected it either alone (from here on referred to as "Control") or together with individual biosensors. Sparse viral labeling via a Cre-lox approach will lead to a handful of virally transfected pyramidal cells with strong fluorescence and minimal background noise. In such a manner, we generated a Cre-dependent version of the H-Ras biosensor and injected it together with Cre proteins in low concentration into layer 2/3 of the primary motor cortex (M1) (Figure 1B). Expression of the Cre protein was regulated under the CaMKII promoter to allow for pyramidal cell specificity.[46] H-Ras
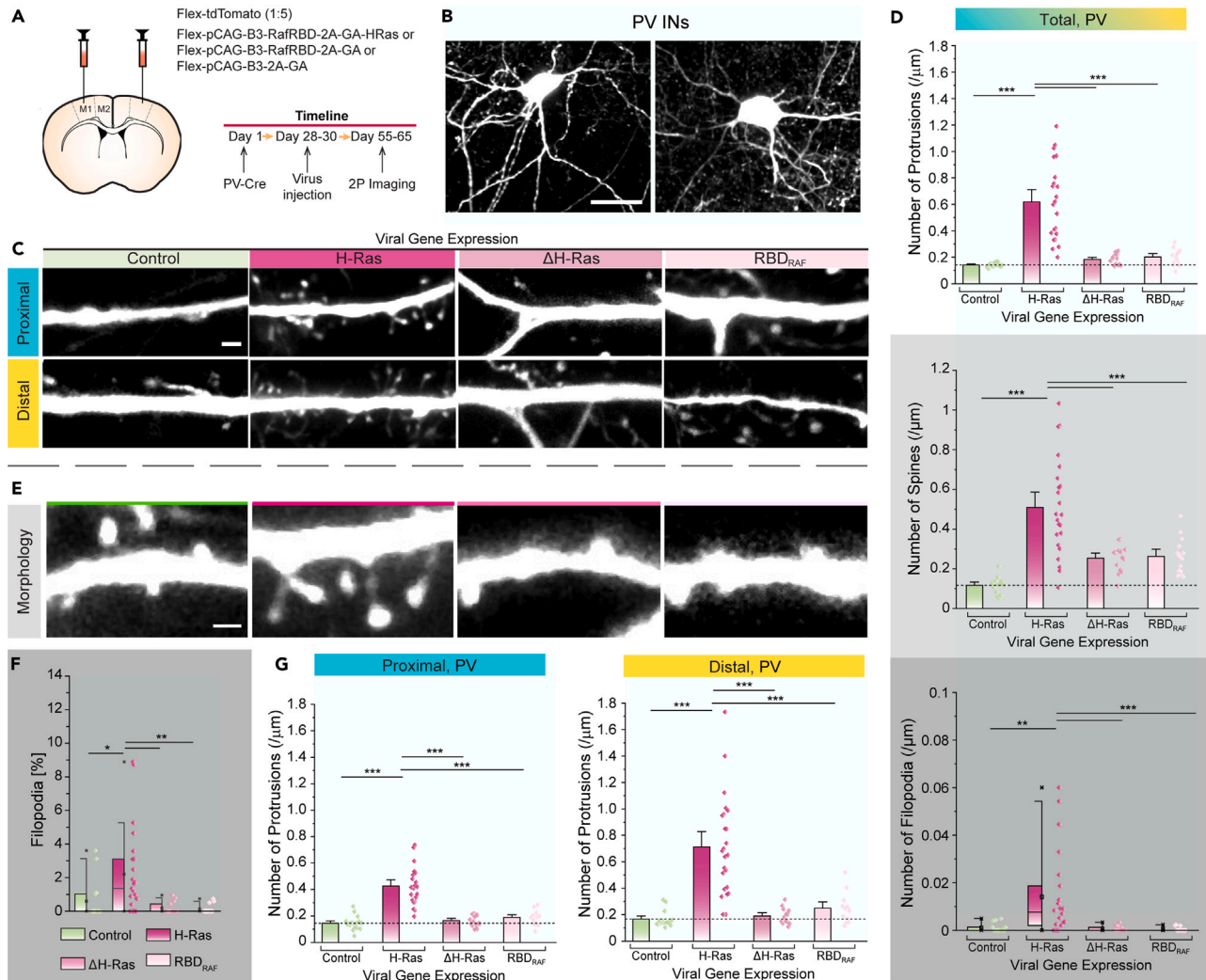
Figure 2. H-Ras increases protrusion number in cortical parvalbumin interneurons

(A) Virus injection scheme and experimental timeline.

(B) Representative two-photon microscopy images of parvalbumin-positive interneurons (PV-INs). Scale bar: 10 μm.

(C) Two-photon microscopy images showing representative dendrites (proximal and distal) of PV-INs expressing Flex-tdTomato and either Flex-pCAG-B3-RafRBD-2A-GA-HRas (H-Ras), Flex-pCAG-B3-RafRBD-2A-GA (RBD$_{RAF}$), or Flex-pCAG-B3-2A-GA (ΔH-Ras). Scale bar, 2 μm.

(D) A superimposed bar and dot graph showing the protrusion, spine, and filopodia density of each neuron (dot) and mean ± SEM (top and middle) or median ± IQR (bottom), respectively, for each condition (control, H-Ras, RBD$_{RAF}$, and ΔH-Ras) in PV INs. The dotted line represents the median or average density of the tdTomato only control. (Top) Protrusion density averaged from all imaged dendritic branches; control (0.14191 ± 0.00433); H-Ras (0.61928 ± 0.06211); ΔH-Ras (0.18324 ± 0.01037); RBD$_{RAF}$ (0.20159 ± 0.01719). control: n = 13; H-Ras: n = 22; ΔH-Ras: n = 14; RBD$_{RAF}$: n = 13. ***p < 0.001 (one-way ANOVA, post-hoc: Tukey test); (Middle) Spine density averaged from all imaged dendritic branches; control (0.11723 ± 0.01079); H-Ras (0.50923 ± 0.05125); ΔH-Ras (0.2538 ± 0.01699); RBD$_{RAF}$ (0.26233 ± 0.02447). Control: n = 15; H-Ras: n = 23; ΔH-Ras: n = 15; RBD$_{RAF}$: n = 14. ***p < 0.001 (one-way ANOVA, post-hoc: Tukey test); (Bottom) filopodia density averaged from all imaged dendritic branches; control (0 ± 0.00132); H-Ras (0.00153 ± 0.01984); ΔH-Ras (0 ± 0.00137); RBD$_{RAF}$ (0 ± 0.00099). Control: n = 16; H-Ras: n = 22; ΔH-Ras: n = 14; RBD$_{RAF}$: n = 13. ***p < 0.001 (Kruskal-Wallis one-way ANOVA, post-hoc: Kolmogorov-Smirnov test).

(E) Representative two-photon images of dendritic protrusions and their morphology. Scale bar = 2 μm.

(F) Graph displaying percentage of filopodia at each expression condition from individual neurons (dots) and the median ± IQR (bar). PV-INs expressing ectopic H-Ras has higher percentages of filopodia.

(G) Separation of protrusion density analysis into proximal and distal. (Left) Protrusion density of proximal dendrites; control (0.14573 ± 0.01189); H-Ras (0.42605 ± 0.03174); ΔH-Ras (0.16542 ± 0.01075); RBD$_{RAF}$ (0.18838 ± 0.01431). Control: n = 18; H-Ras: n = 21; ΔH-Ras: n = 15; RBD$_{RAF}$: n = 14; (Bottom) protrusion density of distal dendrites; control (0.16693 ± 0.01614); H-Ras (0.71365 ± 0.07629); ΔH-Ras (0.19031 ± 0.01679); RBD$_{RAF}$ (0.25007 ±. 0.03138). Control: n = 15; H-Ras: n = 24; ΔH-Ras: n = 13; RBD$_{RAF}$: n = 13. The dotted line represents the average protrusion density of dendrites expressing tdTomato

Figure 2. Continued

only (control). Neurons expressing H-Ras showed a higher rate of dendritic protrusions throughout all dendritic regions. *$p < 0.05$, **$p < 0.01$, ***$p < 0.001$ (two-way ANOVA, post-hoc: Tukey test). Control (green), H-Ras (magenta), ΔH-Ras (light magenta), and RBDRAF (pink). Light shaded box shows graphs related to dendritic spines (D "middle") and dark shaded box shows data related to filopodia (D "bottom" and F).

See also Figures S4 and S5.

expression was confirmed by H-Ras antibody staining showing strong signals in cells expressing the H-Ras biosensor, but only minor endogenous expression in control conditions (Figures S1A–S1C). To count and morphologically characterize dendritic protrusions, we collected acute brain slices and imaged neurons under a two-photon microscope. We identified each protrusion from the selected areas on the dendritic tree letting a semiautomated, custom-made program calculate protrusion count as well as protrusion neck length and head diameter. Any dendritic outgrowth connected to the dendrite and separated from passing axons and dendrites was counted as dendritic protrusion. Unnaturally round fluorescent puncta were excluded representing likely fluorescent artifacts. Average protrusion numbers were significantly higher in pyramidal neurons that expressed H-Ras (>40%) or H-Ras$_{ONLY}$ (>95%) (Figures 1C and 1D). Protrusion numbers between controls were not significantly different and aligned with previously reported spine densities.[8,47,48] Furthermore, the phenotype shifted toward spines with overall longer protrusion necks (Figures S2A–S2C). When classified into filopodia and spines, we uncovered that the increase in protrusions is carried by a rise in filopodia number (Figures 1E–1G). Ectopic H-Ras$_{ONLY}$ expression led to an upsurge in both filopodia and spines, but the effect on spine number was much higher (Figures 1E and 1F) suggesting that co-transfected RBD$_{RAF}$ might have an inhibitory effect on new spine formation. Consequently, the overall percentage of filopodia increased with H-Ras but not with H-Ras$_{ONLY}$ (Figure 1G). Furthermore, in both H-Ras and H-Ras$_{ONLY}$, the observed protrusion elongation extends beyond an increase in filopodia and is also evident in the spine-only fraction (Figures S2D and S2E). This indicates that H-Ras might have additional effects on existing dendritic spines promoting structural modifications.

Next, to determine if the effect on protrusion number is universal or limited to certain regions of the dendritic tree, we segmented the dendrite into three locations (apical proximal, apical distal, and basal) and assessed changes in protrusion distribution based on dendrite class. The most pronounced effect of H-Ras overexpression was observed in apical proximal dendrites (>130%) while basal and apical distal dendrites showed no significant change in protrusion number (Figures 1C and 1H). In comparison, H-Ras$_{ONLY}$ exhibited a protrusion increase in all three dendritic locations, notably surpassing H-Ras's increase in apical proximal and apical distal dendrites (Figures 1C and 1H). Inherently, the protrusion density differs significantly between apical proximal and apical distal dendrites, with lower expressions in apical proximal regions (Figure S3A, "Control"). When H-Ras or H-Ras$_{ONLY}$ were ectopically expressed, this separation disappeared with similar average protrusion numbers no matter the dendritic region (Figure S3A). Indeed, the lack of increase in apical distal dendrites, the modest, but insignificant, increase in basal dendrites, and the big increase in apical dendrites with H-Ras, hints toward an upper limit for protrusion density with average protrusion numbers ranging from ~0.8 to ~1.1 protrusions/μm. However, the maximum protrusion density can be elevated with H-Ras$_{ONLY,}$ where it ranges from ~1.3 to ~1.6 protrusions/μm. Overall, our data show that H-Ras and H-Ras$_{ONLY}$ affect protrusion number and morphology in layer 2/3 PyNs of M1. The surge in protrusion density is attained by an increase in filopodia for H-Ras and a combination of a rise in spine and filopodia number in H-Ras$_{ONLY}$. Although the effect size was bigger in H-Ras$_{ONLY}$, we proceeded to use the H-Ras construct to capitalize on its biosensor activity.

Protrusion density changes by H-Ras ectopic expression are independent of cell types

To assess whether H-Ras produces more dendritic protrusions by directly driving spinogenesis or rather by accelerating their production via existing molecular mechanisms, we expressed H-Ras into PV-INs and VIP-INs where key excitatory synaptic proteins are expected to be absent or low.[43,49,50] The Cre-dependent biosensors and the cell marker were injected into M1 layer 2/3 of PV-Cre and VIP-Cre mouse lines, respectively (Figures 2A and 2B; Figures 3A and 3B). Antibody staining against PV confirmed the selective targeting of PV-INs (Figures S4A–S4C). Protrusion analysis revealed an enormous increase in protrusion number after H-Ras overexpression exhibiting a 300% increase in PV-INs (Figures 2C and 2D) and a 250% increase in VIP-INs (Figures 3C and 3D). The basal spine density levels of our controls were consistent with previous reports.[43,48] We analyzed whether these newly formed protrusions in INs have longer protrusion necks similar to changes in PyNs. Dendritic protrusions in H-Ras overexpressing neurons exhibited longer protrusion necks in PV-INs (Figure 2E, S5A, and S5D) but not VIP-INs (Figures S5C and S5F). As in PyNs, the percentage of filopodia increased in PV INs, although to a lesser extent (Figures 2E and 2F). The change in protrusion neck length was not solitary due to the increase in filopodia since the spine fraction showed an increase in spine neck length independent of filopodia (Figures S5B and S5E). When separating spine and filopodia densities, we noted that both spine and filopodia densities were enhanced, so the increase in protrusions was due to a surge in filopodia as well as spines (Figure 2D). In fact, the increase in spine number was more than 20-fold larger than the increase in filopodia proposing that the increase in dendritic protrusions is predominately driven by an increase in spine density (Figure 2D). VIP INs scarcely developed any filopodia neither in control conditions nor under the influence of H-Ras (Figures 3E and 3F), and the increase in protrusions was carried by dendritic spines (Figure 3E). We suspect that the proteome makeup is different in VIP INs, overall favoring smaller, stubby spines. Even in controls, the morphology of existing spines was shorter in comparison to protrusions from PyNs and PV INs. The difference seen in VIP-INs supports the idea that H-Ras affects cell types in slightly different manners. Consequently, H-Ras might have a dual role in influencing filopodia or spine growth independently based on the environment.

Next, we separated the dendritic tree into two dendrite locations (proximal and distal). When looking at protrusion number increase based on dendrite location, VIP-INs displayed an equal rise in protrusion number throughout the dendritic trees (Figure 3G). PV-INs showed a more
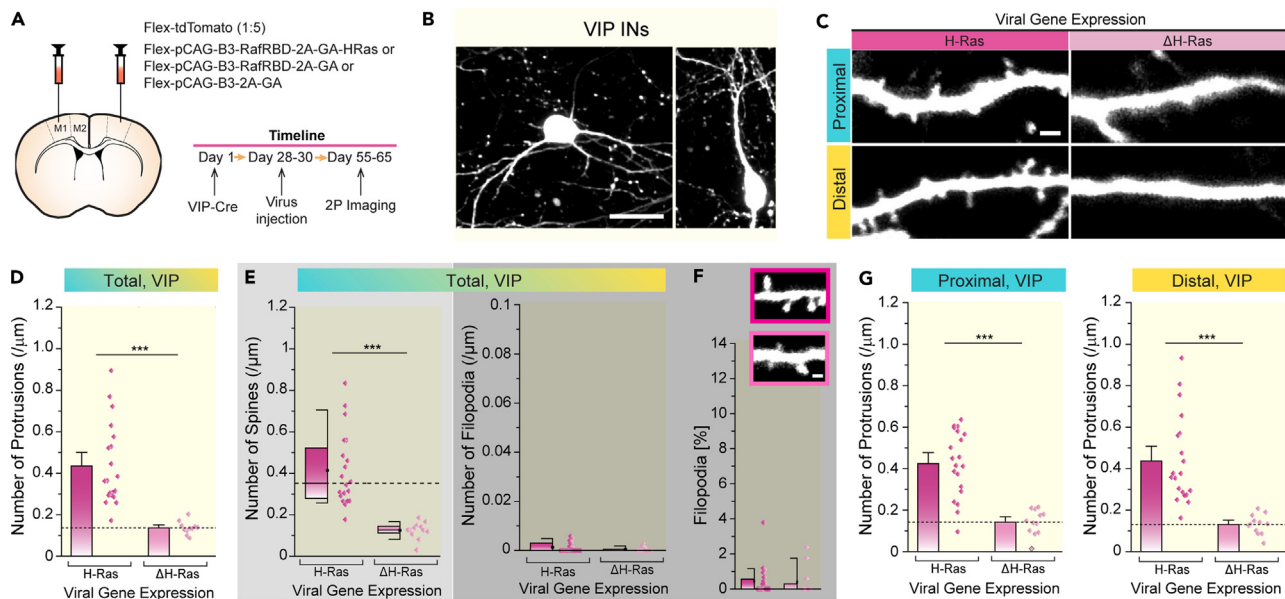
Figure 3. H-Ras increases protrusion number in cortical vasoactive intestinal peptide interneurons

(A) Virus injection scheme and experimental timeline.

(B) Representative two-photon images of vasoactive intestinal peptide-expressing interneurons (VIP-INs). Scale bar: 10 μm.

(C) Two-photon microscopy images showing representative dendrites (proximal and distal) of VIP INs expressing Flex-tdTomato in the primary motor cortex of a typical acute brain slice made from VIP-Cre mice at ~ P60 injected 4-week prior with Flex-tdTomato and either H-Ras, or ΔH-Ras. Scale bar, 2 μm.

(D) A superimposed bar and dot graph showing the protrusion density of each neuron (dots) and mean ± SEM (bar), respectively, for each condition (H-Ras, and ΔH-Ras) in VIP INs; H-Ras (0.43456 ± 0.04397); ΔH-Ras (0.13683 ± 0.13375) H-Ras: n = 20; ΔH-Ras: n = 12; ***$p < 0.001$ (two sample t test).

(E) Separation of protrusion density analysis into spines and filopodia. (Left) Spine density averaged from all imaged dendritic branches; H-Ras (0.42397 ± 0.0354); ΔH-Ras (0.14144 ± 0.0175); H-Ras: n = 22; ΔH-Ras: n = 14. ***$p < 0.001$ (two-sample Kolmogorov-Smirnov test). (Right) Filopodia density averaged from all imaged dendritic branches; H-Ras (0.00298 ± 0.00585); ΔH-Ras (0.00082 ± 0.00291). H-Ras: n = 19; ΔH-Ras: n = 12. ***$p < 0.001$ (two-sample Kolmogorov-Smirnov test).

(F) Graph displaying percentage of filopodia at each expression condition from individual neurons (dots) and the median ± IQR (bar).

(G) Separation of protrusion density analysis into proximal and distal. (Left) Protrusion density of proximal dendrites; H-Ras (0.42397 ± 0.0354); ΔH-Ras (0.14144 ± 0.0175); (Right) protrusion density of distal dendrites; H-Ras (0.43697 ± 0.04737); ΔH-Ras (0.13057 ± 0.01376). The dotted line represents the average protrusion density of dendrites expressing ΔH-Ras. Neurons expressing H-Ras showed a higher protrusion density throughout all dendritic regions. H-Ras: n = 20; ΔH-Ras: n = 12; ***$p < 0.001$ (two sample t test, post-hoc: Sidak Holm's test).

pronounced but equally significant effect in distal (>350%) compared to proximal dendritic segments (>225%) (Figure 2G). These changes are somewhat different from changes in apical distal dendrites of PyNs where there was only a further increase in protrusion numbers with H-Ras$_{ONLY}$ but not H-Ras, suggesting that the precise H-Ras effect may differ between cell types. Moreover, supporting the idea that there could be a cap to the maximum protrusion density as suggested with PyNs, average spine density never exceeded a value above 1 protrusion/μm with ectopic H-Ras expression. H- Ras$_{ONLY}$ was able to lift this effect in PyNs but was not tested in INs.

To sum up, our data show that H-Ras increases protrusion numbers not only in PyNs but also in INs, suggesting that changes in protrusion numbers are not restricted to specific cell types. Nevertheless, the specifics of the newly formed spines and filopodia regarding their density, neck length, and head diameter appear to be cell-type specific. While in PyNs the increase in protrusions highly relies on the increase in filopodia number, PV interneurons show surges in both filopodia and spines. Furthermore, the changes in protrusion densities in VIP interneurons are spine dependent. This suggests a dual role of H-Ras in filopodia formation and spinogenesis. It also implies that the low spine density in INs may be maintained by active cellular processes preventing exuberant spine formation in normal conditions, but this system can be overwritten by ectopic expression of H-Ras allowing a massive formation of dendritic spines. Hence, H-Ras is sufficient to drive spinogenesis.

Local H-Ras activity increases spinogenesis

To examine if increased protrusion number more directly relates to H-Ras activity, we measured H-Ras activity and its correlation with the likelihood of nearby dendritic protrusions. H-Ras biosensor signals appeared dim in acute slice preparations. Additionally, the high number of spines in adult neurons, especially under H-Ras overexpression limits the analysis of spineless regions. For these reasons, we decided to express H-Ras in organotypic slice cultures during early development (EP 9–12) [EP (equivalent postnatal) day = postnatal day at slice culturing + days *in vitro*] where spine number is relatively low (Figures 4A and 4B). DNA bullets containing the H-Ras sensor together with a tdTomato plasmid were transfected to visualize both H-Ras activity and cell morphology from the same neuron (Figures 4A and 4D).
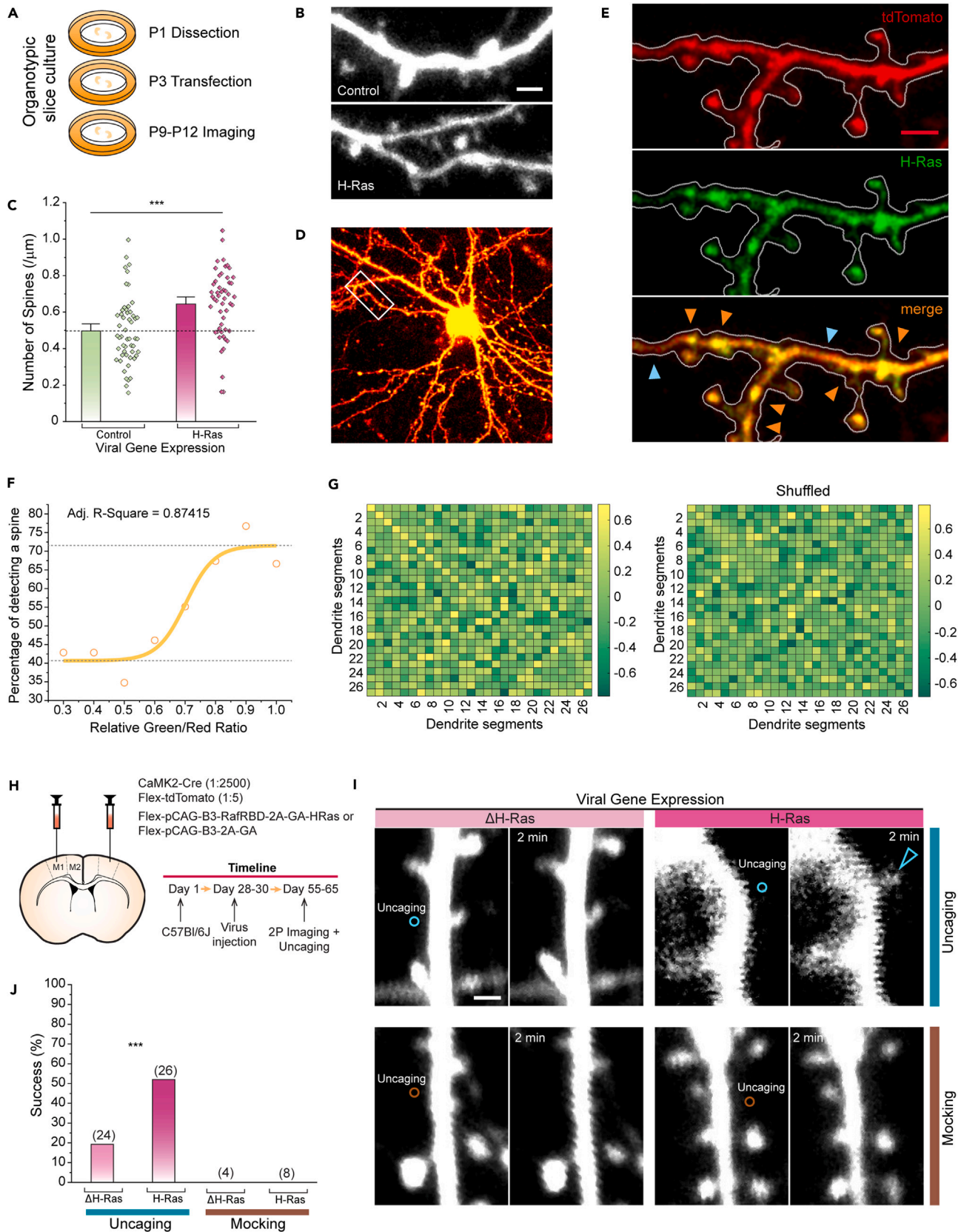
Figure 4. Local H-Ras activity facilitates *de novo* growth of protrusions

(A) Schematic of organotypic slice preparation and timeline.

(B) Representative dendrite images expressing tdTomato (top) and H-Ras (tdTomato + pCAG-B3-RafRBD-2A-GA-HRas) (bottom) collected via a two-photon microscope at P12. DNA was biolistically transfected to organotypic cortical slices at P1. Scale bar: 2 μm.

(C) A summary graph showing the protrusion density of each analyzed dendritic section (∼30 μm) (dots) and the mean protrusion density ± SEM (bar) of Control (0.49719 ± 0.02549) and H-Ras neurons (0.6445 ± 0.02608). The dotted line represents the average protrusion density of control dendrites. Control: n = 53, H-Ras: n = 52; ***$p < 0.001$ (two sample t test).

(D) tdTomato and H-Ras biosensor expression in a representative organotypic pyramidal neuron: red = tdTomato, green = H-Ras biosensor.

(E) Magnification of dendritic branch shown in D (white box) (top) tdTomato, (middle) H-Ras biosensor GFP, and (bottom) merge. Colored arrow heads indicate examples of high H-Ras activity (orange) or low H-Ras activity (light blue). Scale bar: 2 μm.

(F) Scatterplot showing that higher H-Ras activity (relative green/red ratio) correlates with a higher percentage of detecting a spine in close proximity (1 μm). The sigmoidal curve fitting to the data shows an R value of 0.87415.

(G) Correlation matrix comparing H-Ras activity values with the existence of protrusions in a 1 μm radius; (left) experimental data, (right) shuffled data control. H-Ras activity correlates to a higher extent with the existence of dendritic protrusions in the experimental data in comparison to shuffled data.

(H) Virus injection scheme and experimental timeline.

(I) Example images of high-frequency glutamate uncaging (HFU) experiments (circles, 40 pulses at 10Hz) on adult pyramidal neurons (∼P60): (top left) ΔH-Ras + MNI glutamate, (top right) H-Ras + MNI glutamate, (bottom left) ΔH-Ras without MNI-glutamate, and (bottom right) H-Ras without MNI-glutamate. All neurons expressed tdTomato as cell markers. Arrowheads indicate *de novo* spine formation after HFU. Scale bar, 2 μm.

(J) Success rate of *de novo* spine formation by HFU at P60 in pyramidal neurons expressing tdTomato and either ΔH-Ras (19.2%) or H-Ras (52%). In the absence of MNI-glutamate (mock) neither ΔH-Ras nor H-Ras exhibited any *de novo* spine formation. ΔH-Ras: n = 24 trials, 16 cells; H-Ras: n = 26 trials, 15 cells; ΔH-Ras mock: n = 4 trials, 4 cells; H-Ras mock: n = 8 trials, 7 cells. ***$p < 0.001$ (Chi-square test).

See also Figure S5.

Like in acute brain slices, H-Ras overexpression increased protrusion numbers in PyNs (Figures 4B and 4C). H-Ras activity was visible along the dendrite (Figures 4D and 4E). Dendritic segments (40–50 μm) were sectioned into 1 μm subsegments, comparable with the largest observed diameter of dendritic protrusions, and the average H-Ras activity was calculated for each subsegment. Next, we marked each 1 μm segment as a spiny subsegment (1) or a spineless subsegment (0). This ensured that the calculated H-Ras activity was specifically associated with the existence of individual dendritic protrusions. We uncovered that H-Ras activity indeed correlates with the probability of spine existence in a sigmoidal fashion progressing from no correlations at a low range of H-Ras activity, to a strong correlation with high H-Ras activity (Figure 4F). Furthermore, we calculated Pearson pairwise correlations between protrusion profiles and H-Ras activity profiles of each dendrite segment (Figure 4G). We found that correlation was highest when the H-Ras activity profile was compared to the corresponding protrusion profile on the same dendritic segment ("diagonal"). When registered H-Ras signals from one dendritic segment were aligned with protrusion profiles of other dendritic segments ("off-diagonal"), only a weak correlation was detected (Figure 4G "left"). Moreover, when we shuffled protrusion profiles, no correlation was detected even in corresponding dendritic segments (Figure 4G "right"), suggesting that the presence of dendritic protrusions in the position of high H-Ras activity was not simply due to the randomly distributed high protrusion density. Our data show that the distribution of dendritic protrusions was at least partially mirrored by H-Ras activity, implying a role of H-Ras in spinogenesis.

To find additional evidence showing the involvement of H-Ras in protrusion growth, we performed two-photon glutamate uncaging experiments.[17–19,21,22,51] Previous studies showed that glutamate release indirectly triggers an increase in H-Ras activity[33,44] and that a lack of H-Ras significantly reduces the success rate of glutamate-mediated *de novo* spinogenesis.[17] Thus, we hypothesize that activity-dependent and activity-independent protrusion formation share common pathways. By inducing protrusion growth through glutamate uncaging, we aim to investigate the significance and reach of H-Ras. A mixture of Adeno-Associated Virus (AAV) expressing CaMKII-Cre (1:2,500 dilution), Flex-tdTomato, and Flex-pCAG-B3-RafRBD-2A-GA-H-Ras or Flex-pCAG-B3-2A-GA were injected in layer 2/3 PyNs of M1. Acute brain slices were prepared one month after viral injection (Figure 4H) and slices were placed in a recording chamber containing Mg^{2+}-free ACSF with or without 3 mM (4-methoxy-7-nitroindolinyl)-glutamate (MNI-Glu). A brief 720 nm laser pulse (30 pulses at 10 Hz, 4 ms duration) was delivered 0.5 μm away from the dendrite (Figure 4I). Dendritic areas had to be spineless at the uncaging spot and have at least one spine in close vicinity (5 μm) but were otherwise randomly chosen. We found that the success rate of *de novo* protrusion growth was significantly increased when H-Ras was ectopically expressed (Figure 4J). In contrast to our previous findings, but in line with other studies employing glutamate uncaging,[17–22] the new protrusions appeared small and predominately stubby, with a notable absence in filopodia and elongated spine structures. The spine growth was dependent on glutamate release because the same laser pulse failed to induce protrusion growth when MNI-Glu was absent (Figure 4J). Thus, our data strongly suggests that high H-Ras expression mediates the formation of new dendritic spine growth. However, the sufficiency of glutamate release to induce this growth does not rule out that H-Ras induces filopodia and spines intrinsically.

H-Ras increases protrusion dynamics

Increased protrusion density could be achieved not only by more protrusion formation but also by increased stability. To examine protrusion stability, we investigated protrusion turnover rates in layer 2/3 PyNs of M1. We performed time-lapse imaging of dendritic segments every 10 min for a total of 1 h (Figure S6A). We observed the emergence of new protrusions and the disappearance of others, with some reappearing within a mere interval of 10 min. When H-Ras was ectopically expressed, approximately 5 spine changes per 50 μm were registered, consequently reflecting significantly higher protrusion dynamics than the control (Figure S6B). We separated the spine changes into two categories: protrusions that "appeared" and protrusions that "disappeared". Noteworthy, the number of protrusions that newly appeared was
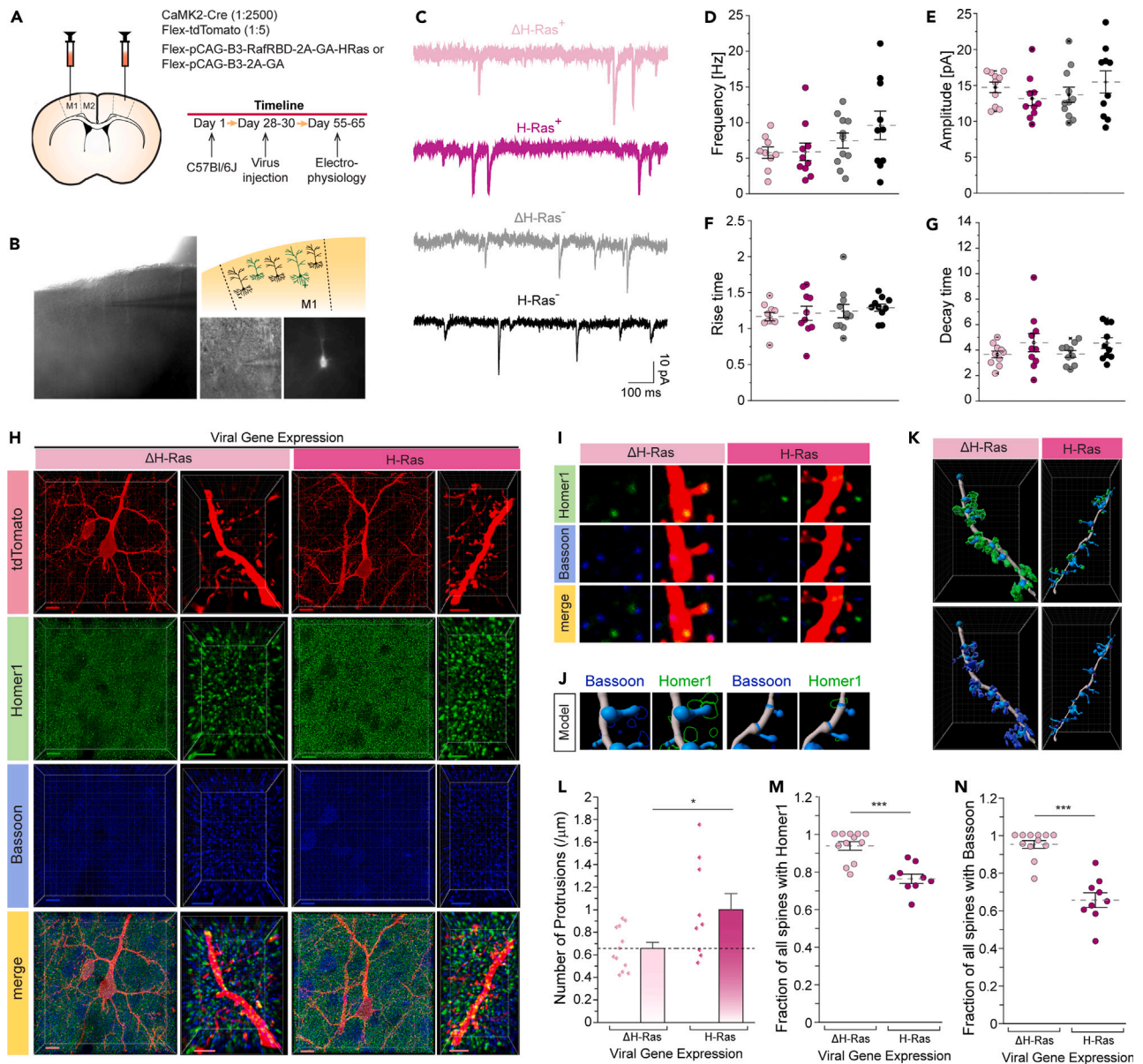
Figure 5. Increased protrusion number does not represent features of functional excitatory synapses

(A) Virus injection scheme and experimental timeline.

(B) Light microscopy images of layer 2/3 pyramidal neuron recorded in whole-cell voltage-clamp-mode in acute slices: whole motor cortical brain region (left), magnified image: light microscopy and fluorescent (right bottom), schematic of pyramidal neurons being fluorescent positive (+) or fluorescent negative (−) (right top).

(C) Examples traces of mEPSCs in ΔH-Ras$^+$ (light magenta), H-Ras$^+$ (magenta), ΔH-Ras$^-$ (gray), and H-Ras$^-$ neurons (black) (1.25 Hz low-pass fft filter).

(D–G) mEPSC frequencies (D), amplitudes (E), rise times (F), and decay time constants (τ) (G) in ΔH-Ras$^+$ (light magenta), H-Ras$^+$ (magenta), ΔH-Ras$^-$ (gray), and H-Ras$^-$ neurons (black). Each dot represents an average value from one neuron, and the dotted line represents mean ± SEM.

(H) Example confocal images of ΔH-Ras and H-Ras of pyramidal neurons (left) and magnified dendrites (right). From top to bottom: image of pyramidal neuron expressing tdTomato, postsynaptic protein Homer1 stained with Alexa Fluor 633 (green), presynaptic protein bassoon stained with Alexa Fluor 405 (blue), merge of all channels. Scale bars: 10 μm (pyramidal neuron), 3 μm (dendrite).

(I) Magnification image of (H) visualizing single protrusions of ΔH-Ras (left) and H-Ras (right). From top to bottom: postsynaptic protein Homer1 (green) stained with Alexa Fluor 633 with and without dendrite visualization, presynaptic protein bassoon with Alexa Fluor 405 (blue) stained with Alexa Fluor 405 with and without dendrite visualization, merge of channels with and without dendrite visualization. Scale bar: 0.75 μm.

(J) Imaris reconstructed image of dendrites and dendritic protrusions in conjunction with bassoon reconstruction (blue) or Homer1 reconstruction (green) of ΔH-Ras (left) and H-Ras neurons (right). Scale bar: 0.75 μm.

(K) Imaris reconstruction of dendrites/protrusions together with Homer1 (green, top) or bassoon (blue, bottom) of ΔH-Ras (left) and H-Ras neurons (right).

Figure 5. *Continued*

(L) A summary graph showing the protrusion density of PyNs with confocal imaging. ΔH-Ras: n = 12, H-Ras: n = 9; *$p < 0.05$ (two-sample t test).

(M and N) Analysis of fraction of protrusions having close contact (0.1 μm) to bassoon puncta (M) or encompassing Homer1 puncta (N) in either ΔH-Ras or H-Ras neurons shows that neurons expressing ectopic H-Ras have reduced number of protrusions expressing Homer1 as well as reduced bassoon contacts. ΔH-Ras: n = 12, H-Ras: n = 9; **$p < 0.01$, ***$p < 0.001$ (two-sample Kolmogorov-Smirnov test).

See also Figures S7 and S8.

significantly enhanced from the control; however, the number of protrusions that disappeared was not significantly different. This suggests that H-Ras plays a major role in producing more dendritic protrusions rather than making existing protrusions more stable (Figure S6C).

Increased filopodia and spine numbers do not represent features of functional excitatory synapses

We next sought to determine whether the exuberant number of protrusions following H-Ras overexpression in PyNs, predominately categorized as filopodia, are coupled with functional synaptic changes. To test functional connectivity changes, we measured miniature excitatory postsynaptic currents (mEPSCs) in layer 2/3 PyNs of M1 (Figures 5A and 5B). Changes in mEPSC frequency are thought to reflect a shift in functional synapse number.[52] In our case, an increase would correlate with a rise in functional filopodia, while a reduced or unchanged mEPSC frequency would point toward silent, non-functional filopodia. Post-hoc analyses showed that there was no difference in mEPSC frequency, amplitude, rise time, or decay tau between control and H-Ras conditions (Figures 5C–5G), arguing against the notion that the newly formed filopodia are functional excitatory synapses. This result seems to be in line with recent studies demonstrating the existence of silent filopodia in the adult neocortex.[16,28]

We also examined whether dendritic spines and filopodia possessed key pre- and postsynaptic proteins. We used antibodies against the postsynaptic scaffolding protein Homer1, which is involved in glutamate receptor targeting, and the presynaptic scaffolding protein bassoon, which assembles at the active zone and is involved in neurotransmitter release. Homer1 comes in three isoforms with its two most abundant isoforms exclusively expressed in the postsynaptic density (PSD), a hallmark for mature spines.[53–55] Antibody-stained neurons were imaged with a confocal microscope, images were deconvoluted (Figure S7A) and neuronal structures, bassoon and Homer1 puncta were subsequently reconstructed via Imaris software (Figure S7B). Image analysis was performed by identifying protrusions colocalized with Homer1 or bassoon in first-order dendritic branches (Figure 5H). First, we confirmed that the increase in protrusions with H-Ras overexpression was detectable via confocal imaging (Figure 5L). Since we could not distinguish between preexisting and new H-Ras-induced protrusions, we selected the entire dendritic spine and filopodia population to calculate the fraction of protrusions containing Homer1 or bassoon. The presence of Homer1 or bassoon signal close to or inside spine or filopodia heads was counted as colocalization (within 0 μm from the spine head for Homer1 and 0.1 μm for bassoon) (Figures 5I and 5J). We found that the number of protrusions was increased by H-Ras expression (Figure 5L), but significantly fewer protrusions contained Homer1 in H-Ras transfected neurons (Figures 5K and 5M), suggesting protrusions lacking Homer1 were induced by H-Ras ectopic expression. However, we cannot exclude that H-Ras destabilizes preexisting spines. Previously reported silent spines lack AMPA (α-amino-3-hydroxy-5-methyl-4-isoxazoleproprionic acid) type receptors but show normal presynaptic connectivity.[28,56,57] We checked if H-Ras-induced protrusions form presynaptic networks even though they are postsynaptically immature. Consistent with Homer1 data, the fraction of protrusions innervated by bassoon was significantly lower with H-Ras overexpression suggesting that H-Ras-induced protrusions fail to build connections with presynaptic partners (Figures 5K and 5N).

Since the increase in protrusions in PyNs was mostly carried by filopodia, we were not surprised that many protrusions were non-functional and without presynaptic partners. Taking into consideration that newly formed protrusions in PV and VIP INs consisted of filopodia as well as spines, we conducted mEPSC recordings in INs (Figures S8A and S8F). Same as in PyNs there was no change in mEPSC frequency, amplitude, rise time, or decay tau when H-Ras was ectopically expressed (Figures S8B–S8E and S8G–S8J). Overall, the results suggest that protrusions generated by H-Ras even if they look like normal, functional dendritic spines are not functionally active.

DISCUSSION

Dendritic spines are structural components of most mammalian glutamatergic synapses.[58–60] In this study, we overexpressed H-Ras in layer 2/3 PyNs, PV INs, and VIP INs and investigated its influence on protrusion number, morphology, turnover rate, and functionality. We observed an increase in protrusion numbers across all neuron types, suggesting a robust and widespread response. The most unexpected changes were found in INs and proximal apical dendrites of PyNs, regions known for their sparse excitatory synapse numbers. Protrusion turnover rates in PyNs revealed that H-Ras enhanced plasticity by accelerating new protrusion formation rather than stabilizing preexisting ones. In INs, the protrusion density increased by 200–300% compared to control conditions. Such dramatic changes led us to question whether H-Ras-induced dendritic protrusions are indeed capable of playing a functional role. We hypothesize that the induced protrusions differ from functional preexisting spines. This is supported by mEPSC recordings, where we revealed no functional change in amplitude or frequency. Additionally, we observed that H-Ras induced dendritic protrusions resemble filopodia in morphology in PyNs and PV INs, but not VIP INs, and lack key pre- and postsynaptic proteins. Upon categorizing the protrusions into filopodia and spines, we noted a predominant surge in filopodia in PyNs, whereas VIP INs showed a prominent increase in dendritic spines without any change in filopodia. On the other hand, PV INs exhibited an increase in both filopodia and dendritic spines. This suggests that H-Ras plays a cell type-independent role in protrusion formation, while the fate of protrusions to develop into filopodia or dendritic spines is cell-type specific. We speculate that the protrusion increase in PyN may not be as pronounced as in INs due to the abundance of preexisting spines, potentially limiting the available space for additional

protrusions. In support of this proposed ceiling effect, average protrusion densities in PyNs, PV INs, and VIP INs never exceeded a value of 1 protrusion per μm, reinforcing the idea that there could be a cap to the maximum protrusion density. To our surprise, when the RBD domain was deleted, leaving only the H-Ras protein in the construct, the maximum protrusion density was elevated to 1.5 protrusions per μm. This suggests that the RBD domain interacts with other Ras effectors, potentially playing a role in suppressing protrusion formation. It appears that this inhibitory effect was masked by the overexpression of H-Ras.

H-Ras as primer molecule for new protrusion formation

Our findings align with previous studies suggesting that H-Ras plays a role as primer for synaptic plasticity. Within the realm of motor behavior, several studies demonstrated that motor learning induces the formation of new spines in a non-random fashion in PyNs, with a tendency for these new spines to cluster near preexisting stable spines involved in the task.[1,27–29] Preexisting spines show signs of recent structural plasticity suggesting that signaling molecules spread from the stimulated spine to nearby dendritic segments priming the area for *de novo* spine formation.[17,27,28] H-Ras is known to be upregulated during LTP and can travel to neighboring dendritic regions (10 μm) staying active for ~5 min at a time.[33] These findings led us to investigate H-Ras as a promising candidate for a spreading, spinogenic molecule or "primer molecule".

In our study, H-Ras overexpression alone was able to induce a surge in filopodia density in PyNs. Filopodia are abundant during development, comprising approximately 12% of all dendritic protrusions in the cortex but rare in adulthood.[14] In developing mouse neocortical neurons, a considerable number of new filopodia are generated daily (~50,000). When compared to the total number of generated spines (~2,000), filopodia may engage in spatial sampling. This implies that the energy expended on filopodia production and retraction is likely related to synaptogenesis, a critical challenge for developing neurons to solve. A compelling body of evidence led us to the current understanding of filopodia as precursors to dendritic spines, representing a continuum of morphologically plastic structures rather than distinct entities with separate processes and functions.[9,61,62] Interestingly, a recent study suggests that conventional microscopy techniques may underestimate the prevalence of filopodia in adulthood,[16] bolstering earlier claims that during learning spine formation is preceded by the generation of a significant amount of filopodia, which are initially silent, but can be recruited for new synaptic connections.[16,28,29] In our study, filopodia were formed by an intrinsic mechanism involving H-Ras. In support of this H-Ras primer hypothesis, we were able to detect correlations between H-Ras activity and protrusions using our H-Ras biosensor. We revealed that the probability of detecting a spine was higher in a 1 μm radius from a dendritic region with high H-Ras activity, than in dendritic segments that displayed low H-Ras activity. However, H-Ras is freely diffusible along the membrane; therefore, it is probable that the correlation between protrusion density and H-Ras activity was due to the presence of high H-Ras activity in dendritic regions with high surface-to-volume ratio.

We found more direct evidence of H-Ras involvement in spinogenesis using two-photon photolysis, where focal, repetitive release of glutamate near the dendrite was able to induce *de novo* spine formation at a higher success rate in the presence of ectopic H-Ras expression. Given that H-Ras exhibits heightened sensitivity to downstream signaling during LTP,[33,44] we hypothesize that a higher availability of H-Ras is indicative of a higher amount of active H-Ras after glutamate photolysis. Consequently, this results in a higher success rate of *de novo* spine formation. In theory, active H-Ras would travel to nearby dendritic areas and induce the growth of new filopodia. However, we observed that *de novo* spinogenesis via two-photon photolysis often bypassed the filopodia stage, and protrusions transitioned directly into mushroom spines, in accordance with previous reports.[17,18] It remains unclear whether the observation of direct spinogenesis without filopodia precursors accurately represents reality or if potential resolution issues are causing us to overlook the filopodia stage. A more radical interpretation is that the success of glutamate photolysis relies solely on its focal uncaging spot coinciding with filopodia that are present, but invisible to the microscope. Regardless, H-Ras appears to lower thresholds and expedite the formation of new dendritic spines following glutamate photolysis, while the intermediate state of filopodia may or may not be a prerequisite for spine formation. Overall, we think that activity-dependent spinogenesis and cell-intrinsic mechanisms for spine formation are not mutually exclusive.

H-Ras enhances synaptic plasticity via its downstream pathways

Proteins of the Ras family act as intermediaries between extracellular signaling and the actin cytoskeleton.[63,64] H-Ras not only exerts immediate local effects upon activation but also initiates global, more long-term effects by triggering downstream translational and transcriptional changes, possibly altering the overall protein makeup of neurons.[65,66] Expression of a constitutively active form of Ras and administration of BDNF, an upstream effector of H-Ras, independently, led to an increase in filopodia number with reduction in spine number.[34] Ras possesses two effector domains: RAF and PI3K. Constitutive activation of only the H-Ras-RAF pathway resulted in minimal reduction of spine number, while constitutive activation of only the H-Ras-PI3K pathway caused no change in spine number.[34] It is well known that protrusion phenotypes and initial outgrowth are actin-dependent, and although actin itself does not have many isoforms, its versatility and adaptability arise from the proteins it binds.[67,68] A cell culture study demonstrated that interaction between the actin-binding protein Drebrin and Ras destabilizes existing mature spines, causing them to lose presynaptic contacts and transition into immature dendritic filopodia.[69] In line with this, H-Ras knockdown experiments showed enhancements in synaptic responses and LTP, suggesting a transition toward greater stability in the absence of H-Ras.[70] Similarly, siRNA against Ras prevented drebrin-induced destabilization of dendritic spines.[69] Thus, H-Ras may regulate binding of drebrin to actin filaments, shifting the balance from stability to plasticity.

In our study, spine turnover rates and elongation of protrusions confirmed a shift toward higher dendritic protrusion plasticity following H-Ras overexpression. Notably, the earlier described constitutively active Ras studies utilized a mixture of Ras proteins, not solely H-Ras. Hence, small discrepancies, such as the higher extent of spine-to-filopodia transformation in earlier studies and the lack of overall protrusion

increase, can be attributed to the variation in Ras proteins. Moreover, there were other differences in experimental conditions, including the reduced complexity of cell cultures, the younger age of neurons, and the fact that Ras was constitutively active in previous studies,[34,69] that might also account for discrepancies. These differences might explain why preexisting spines were largely unaffected in our study, although we cannot entirely exclude the possibility of destabilization of preexisting spines. The absence of protrusion reduction in H-Ras knockdown experiments, however, was surprising.[71] As H-Ras knockdown has only a mild effect on protrusion number, these studies suggest that compensatory mechanisms, likely involving other isoforms of Ras proteins such as N-Ras or K-Ras, take over the function of H-Ras. Indeed, downstream effectors of H-Ras seem to be normally regulated after prolonged absence of H-Ras.[71] In the future, it would be interesting to explore the acute effects of H-Ras knockdown. Moreover, it is worth considering whether a knock-out of all Ras isoforms could yield similar outcomes although such an experiment could not be performed *in vivo* due to embryonic lethality.

Interestingly, protrusions on VIP INs did not appear to transition to elongated spines and filopodia. Naturally, we were curious whether mRNA and protein levels of drebrin were different in VIP INs. Utilizing the searchable web interface that accesses transcriptomic datasets (https://research-pub.gene.com/NeuronSubtypeTranscriptomes)[50] and the Allen Brain Transcriptomics Explorer (https://celltypes.brain-map.org/rnaseq/mouse_ctx-hpf_10x),[72] we observed that drebrin mRNA levels were overall lower in both VIP and PV INs. According to the Allen Brain Transcriptomics explorer, VIP INs completely lack any drebrin mRNA, while PV INs exhibit low levels, and PyNs express high levels. Earlier findings showed that RNAi-mediated drebrin knockdown prevented Ras-induced spine elongation and destabilization.[69] Hence, the absence of drebrin together with the absence of elongated spines in VIP INs in our study could be related. Considering that VIP INs still showed an increase in spine number, we hypothesize a secondary mode of action of H-Ras that does not rely on drebrin. Many genes encoding actin binding and bundling proteins like fascin, profilin, and components of the ARP2/3 complex are known to be involved in the outcropping of dendritic segments.[67,68] It is conceivable that H-Ras induces protrusion growth directly via interacting with other actin-related proteins or indirectly via its translational and transcriptional effects, possibly altering the intrinsic protein balance.

Interneurons and their innate low spine density

Only a few molecules involved in dendritic spine formation in INs have been identified. One study reported that the overexpression of the extracellular N-terminal domain of AMPA receptor subunit GluA2 increased spine number in GAD-positive neurons.[73] However, these experiments were only performed in embryonic culture neurons and findings were demonstrated by only a few sample images. This result is also not compatible with a more recent study showing that spine density was completely normal even when all subunits of AMPARs and N-methyl-D-aspartate receptors (NMDARs) were deleted.[26] Therefore, mechanistic understanding of spine formation in INs is still elusive. The current study posits a permissive role of H-Ras in protrusion outgrowth in both PyNs and INs. The fact that over expression of H-Ras induces a high number of dendritic spines in INs implies that the reason for maintaining the low density of dendritic spines in INs could be due to the absence of H-Ras, or alternatively that other mechanism competes with H-Ras activity, precluding spine growth. Browsing the searchable web interface that accesses transcriptomic datasets[50] and the Allen Brain Transcriptomics Explorer,[72] we found that H-Ras mRNA levels were significantly reduced in VIP INs compared to PyNs. In PV INs, this effect was only minimal and not consistent throughout different purification and RNA-sequencing techniques, suggesting that there might be other factors influencing low spine numbers. Pinpointing the exact proteins, however, is a difficult challenge to solve, as many genes are differentially regulated in INs.

Separation between spinogenesis and synaptogenesis

Our data further shows that the exuberant protrusions were not functionally incorporated into the pre-existing neural network. Upregulation of functional spines alters physiological properties of neurons, with more spines leading to a higher frequency of miniature excitatory post-synaptic currents (mEPSCs).[52] This change in mEPSC frequency was absent in H-Ras expressing layer 2/3 PyNs and PV and VIP INs of M1, indicating that the exuberant filopodia in PyNs and dendritic spines in PV and VIP INs are pre- and postsynaptically silent. Silent dendritic spines were labeled as"protospines". Supporting our electrophysiology findings, protrusions in H-Ras transfected PyNs were devoid of key postsynaptic molecules, reflected by the absence of Homer1 in ~25% of protrusions. Even though we are unable to distinguish between H-Ras induced and pre-existing protrusions, the fraction of protrusions without Homer1 was comparable to the fraction of new protrusions. We must keep in mind, however, that one of the three isotypes of Homer1, Homer1a, is not bound to the PSD and is instead present in the cytosol and found in both mature and immature spines,[53] suggesting that the actual number of immature protrusions may be higher. Our antibody staining against the presynaptic marker bassoon revealed that about 35% of protrusions (comparable with the 35% protrusion increase) lacked bassoon signal after H-Ras overexpression.

Since the dendritic protrusions formed via ectopic H-Ras expression in PyNs and INs seem to not build functional synapses, at least not immediately, this opens the door for speculations concerning the role of H-Ras *in vivo*. H-Ras may serve as a regulator between stability and plasticity by dynamically regulating the formation of filopodia in PyNs. Filopodia induction might need to be held in delicate balance: while some filopodia may transition into functional spines, an overabundance of filopodia might compete for molecular resources, compromising the functionality of neighboring dendritic spines. Arstikaitis et al. demonstrated that filopodia stabilization rather than filopodia number is the rate-limiting factor for synapse formation.[74] Therefore, overproduction of filopodia could have dual effects: enhancing the likelihood of maturation into functional spines while simultaneously destabilizing existing spines by depleting molecular resources. Furthermore, the switch to stability could be inversely controlled by the continuous activity of H-Ras, explaining why filopodia and "protospines" are functionally silent. We propose that the balance between H-Ras's "on"- and "off"-state ensures the induction of new filopodia and "protospines" ("on"-state), which could then be recruited for learning and memory ("off"-state).

H-Ras and its involvement in tunneling nanotubes

Could these protrusions have another purpose? The lack of presynaptic partners in H-Ras induced protrusions contrasts with findings of an earlier study, where filopodia were postsynaptically silent but were still integrated in the synaptic network.[16] Interestingly, filopodia occur in neurons that do not have spines at maturity,[75,76] and even in many non-neuronal cells.[14,77] While proteins of the Ras family appear to influence filopodia outgrowth in fibroblasts and certain cancer cells,[78,79] it would be presumptuous to assume that Ras's effect in non-neuronal cells and neurons is the same. Hence, filopodia are believed to be versatile with multiple functions beyond their role as spine precursors, such as facilitating cell-cell communication,[77] regulating cellular mobility, and promoting dendritic tree outgrowth.[15,80] In certain cell types, such as PC12 cells, HeLa cells, microglia, astrocytes, and pericytes, intercellular connections can form through structures known as tunneling nanotubes, through which the cells can exchange nutrients, and small molecules.[77,81–85] Conventional microscopes struggle to resolve these extremely thin and transient structures. Hence, a super-resolution setup is optimal to study them. Tunneling nanotube connections were shown to arise from filopodia outgrowths where two filopodia from two different cells form a filopodia bridge.[77] These tunneling nanotubes are close-ended and communicate through gap junctions consistent with connexin 43 expression at the tunneling nanotube endfeet.[77,83] Tunneling nanotubes formed between B and T immune cells were enriched for H-Ras suggesting that H-Ras may be transported through these nanotubes as cargo or is involved in their construction.[86] Upon revisiting a gene analysis study from 2003, we uncovered that connexin 43 is one of the genes highly enriched in fibroblasts expressing constitutively active H-Ras$_{G12V}$. Intercellular communication is fundamental to brain function. Thus, it was not surprising that tunneling nanotubes were discovered between photoreceptors and between neurons and astrocytes.[81,82,87] Although tunneling nanotubes between neurons in the neocortex have not been described, the abundance of filopodia in these cells suggests that similar intercellular communication structures may exist. Hence, we surmise that H-Ras may play a key role in the formation of these tunneling nanotubes, potentially contributing to intercellular communication in neuronal networks. More research is needed to investigate this idea and unravel the precise mechanisms involved.

Our data uncovered that dendritic spines can be induced without causing functional synaptic connectivity changes. The spine-synapse dissociation and robust increase of dendritic spines in INs suggest that dendritic spines may not be just created as one-half of a synapse. There might be a crossroad where the fate of these protrusions is decided, and it is determined whether they will develop into dendritic spines or other structures like tunneling nanotubes.

Limitations of the study

We used two-photon microscopy in our study. However, recent studies combining light and electron microscopy have shed light on some of the limitations of conventional light microscopy in capturing small, thin structures such as filopodia, which may be obscured by the fluorescence surrounding dendrites and larger spines.[16,28,30] As a result, the generation and subsequent transition of certain filopodia into spines may not be observable using our current methods. More rigorous microscopy techniques such as electron microscopy, may be necessary to observe these structures accurately. Unfortunately, timelapse imaging and high-frequency uncaging cannot be performed with electron microscopy. Another limitation lies in the characterization of filopodia, as the definition of filopodia varies depending on the literature. The primary challenge arises from the morphological characteristics of continuous membrane protrusions from dendrites with varying lengths of spine neck. Additionally, accurately measuring the size of spine heads or the thickness of spine necks under two-photon microscopy is difficult due to the diffraction limit of microscopy. Consequently, the definition of filopodia remains subjective. For our study, we defined filopodia as dendritic protrusions with a length greater than 3.5 μm and lacking a clear dendritic spine head. Furthermore, the precise molecular mechanisms of how H-Ras induces *de novo* filopodia and spines were not the focus of this study and need to be investigated in follow-up studies. We used transcriptomics databanks to discuss certain molecular mechanisms possibly involved in filopodia and spine formation in PyNs, PV INs, and VIP INs. Unfortunately, functional information is often limited in transcriptomics studies, due to substantial discordance between mRNA and protein levels, especially in neurons.[88–91] Proteomics studies would give more insights yet remain scarce due to technical constraints. Recent advances in spatial proteomics and the development of proteomic tags capable of labeling cell-type specific proteomes will provide promising tools to advance candidate targets.[91,92]

STAR★METHODS

Detailed methods are provided in the online version of this paper and include the following:

- KEY RESOURCES TABLE
- RESOURCE AVAILABILITY
  - Lead contact
  - Materials availability
  - Data and code availability
- EXPERIMENTAL MODEL AND SUBJECT DETAILS
  - Animals
  - Tissue culture
- METHODS DETAILS
  - Animal surgery and viral stereotaxic injection
  - Preparation of acute cortical slices

- ○ Two-photon imaging
- ○ Glutamate uncaging
- ○ Electrophysiology
- ○ Immunohistochemistry and confocal imaging
- ● QUANTIFICATION AND STATISTICAL ANALYSIS
- ○ Structural imaging analysis
- ○ Immunohistochemistry image analysis
- ○ Statistics

SUPPLEMENTAL INFORMATION

Supplemental information can be found online at https://doi.org/10.1016/j.isci.2024.110535.

AUTHOR CONTRIBUTIONS

S.K. and H.-B.K. conceived and designed the study. S.K. and I.D. performed viral injection for experiments. S.K prepared organotypic slices. S.K. performed two-photon imaging, two-photon uncaging, and electrophysiology recording. S.K. and I.D. performed immunohistochemistry and confocal imaging. M.C. wrote spine morphology data analysis and deconvolution program. S.K. wrote correlation analysis program. S.K. analyzed spine density, morphology, dynamics, correlation, and electrophysiology data. I.D. provided assistance in spine morphology analysis. I.D and S.K. analyzed histology data. S.S. provided Cre-dependent versions of the H-Ras biosensor. H.-K.L., G.E., and W.-D.H. provided critical advice on the manuscript. S.K. and H.-B.K. wrote the manuscript, and S.K., H.-B.K., and G.E. edited the manuscript. All authors discussed and commented on the manuscript.

DECLARATION OF INTERESTS

The authors declare no conflict of interest.

REFERENCES

1. Fu, M., Yu, X., Lu, J., and Zuo, Y. (2012). Repetitive motor learning induces coordinated formation of clustered dendritic spines in vivo. Nature *483*, 92–95. https://doi.org/10.1038/nature10844.

2. Grutzendler, J., Kasthuri, N., and Gan, W.B. (2002). Long-term dendritic spine stability in the adult cortex. Nature *420*, 812–816. https://doi.org/10.1038/nature01276.

3. Holtmaat, A.J.G.D., Trachtenberg, J.T., Wilbrecht, L., Shepherd, G.M., Zhang, X., Knott, G.W., and Svoboda, K. (2005). Transient and persistent dendritic spines in the neocortex in vivo. Neuron *45*, 279–291. https://doi.org/10.1016/j.neuron.2005.01.003.

4. Lai, C.S.W., Franke, T.F., and Gan, W.B. (2012). Opposite effects of fear conditioning and extinction on dendritic spine remodelling. Nature *483*, 87–91. https://doi.org/10.1038/NATURE10792.

5. Peters, A.J., Chen, S.X., and Komiyama, T. (2014). Emergence of reproducible spatiotemporal activity during motor

learning. Nature *510*, 263–267. https://doi.org/10.1038/NATURE13235.

6. Trachtenberg, J.T., Chen, B.E., Knott, G.W., Feng, G., Sanes, J.R., Welker, E., and Svoboda, K. (2002). Long-term in vivo imaging of experience-dependent synaptic plasticity in adult cortex. Nature *420*, 788–794. https://doi.org/10.1038/NATURE01273.

7. Xu, T., Yu, X., Perlik, A.J., Tobin, W.F., Zweig, J.A., Tennant, K., Jones, T., and Zuo, Y. (2009). Rapid formation and selective stabilization of synapses for enduring motor memories. Nature *462*, 915–919. https://doi.org/10.1038/nature08389.

8. Yang, G., Pan, F., and Gan, W.B. (2009). Stably maintained dendritic spines are associated with lifelong memories. Nature *462*, 920–924. https://doi.org/10.1038/nature08577.

9. Zuo, Y., Lin, A., Chang, P., and Gan, W.B. (2005). Development of long-term dendritic spine stability in diverse regions of cerebral cortex. Neuron *46*, 181–189. https://doi.org/10.1016/J.NEURON.2005.04.001/

ATTACHMENT/EF1777DA-F961-4D88-9C55-C4613079BF1A/MMC1.PDF.

10. Chih, B., Engelman, H., and Scheiffele, P. (2005). Control of excitatory and inhibitory synapse formation by neuroligins. Science *307*, 1324–1328. https://doi.org/10.1126/SCIENCE.1107470/SUPPL_FILE/CHIH.SOM.PDF.

11. Chubykin, A.A., Liu, X., Comoletti, D., Tsigelny, I., Taylor, P., and Südhof, T.C. (2005). Dissection of synapse induction by neuroligins: effect of a neuroligin mutation associated with autism. J. Biol. Chem. *280*, 22365–22374. https://doi.org/10.1074/jbc.m410723200.

12. Graf, E.R., Zhang, X., Jin, S.X., Linhoff, M.W., and Craig, A.M. (2004). Neurexins induce differentiation of GABA and glutamate postsynaptic specializations via neuroligins. Cell *119*, 1013–1026. https://doi.org/10.1016/j.cell.2004.11.035.

13. Ko, J., Fuccillo, M.V., Malenka, R.C., and Südhof, T.C. (2009). LRRTM2 Functions as a Neurexin Ligand in Promoting Excitatory Synapse Formation. Neuron *64*, 791–798.

https://doi.org/10.1016/J.NEURON.2009.
12.012.

14. Yuste, R., and Bonhoeffer, T. (2004). Genesis of dendritic spines: Insights from ultrastructural and imaging studies. Nat. Rev. Neurosci. *5*, 24–34. https://doi.org/10.1038/nrn1300.

15. Wit, C.B., and Hiesinger, P.R. (2023). Neuronal filopodia: From stochastic dynamics to robustness of brain morphogenesis. Semin. Cell Dev. Biol. *133*, 10–19. https://doi.org/10.1016/J.SEMCDB.2022.03.038.

16. Vardalaki, D., Chung, K., and Harnett, M.T. (2022). Filopodia are a structural substrate for silent synapses in adult neocortex. Nature *612*, 323–327. https://doi.org/10.1038/s41586-022-05483-6.

17. Kwon, H.B., and Sabatini, B.L. (2011). Glutamate induces de novo growth of functional spines in developing cortex. Nature *474*, 100–104. https://doi.org/10.1038/nature09986.

18. Oh, W.C., Lutzu, S., Castillo, P.E., and Kwon, H.B. (2016). De novo synaptogenesis induced by GABA in the developing mouse cortex. Science *353*, 1037–1040. https://doi.org/10.1126/science.aaf5206.

19. Guo, L., Xiong, H., Kim, J.-I., Wu, Y.-W., Lalchandani, R.R., Cui, Y., Shu, Y., Xu, T., and Ding, J.B. (2015). Dynamic rewiring of neural circuits in the motor cortex in mouse models of Parkinson's disease. Nat. Neurosci. *18*, 1299–1309. https://doi.org/10.1038/nn.4082.

20. Wu, M., Minkowicz, S., Dumrongprechachan, V., Hamilton, P., and Kozorovitskiy, Y. (2021). Ketamine Rapidly Enhances Glutamate-Evoked Dendritic Spinogenesis in Medial Prefrontal Cortex Through Dopaminergic Mechanisms. Biol. Psychiatry *89*, 1096–1105. https://doi.org/10.1016/j.biopsych.2020.12.022.

21. Hamilton, A.M., Oh, W.C., Vega-Ramirez, H., Stein, I.S., Hell, J.W., Patrick, G.N., and Zito, K. (2012). Activity-Dependent Growth of New Dendritic Spines Is Regulated by the Proteasome. Neuron *74*, 1023–1030. https://doi.org/10.1016/J.NEURON.2012.04.031.

22. Kozorovitskiy, Y., Saunders, A., Johnson, C.A., Lowell, B.B., and Sabatini, B.L. (2012). Recurrent network activity drives striatal synaptogenesis. Nature *485*, 646–650. https://doi.org/10.1038/nature11052.

23. Sigler, A., Oh, W.C., Imig, C., Altas, B., Kawabe, H., Cooper, B.H., Kwon, H.-B., Rhee, J.-S., and Brose, N. (2017). Formation and Maintenance of Functional Spines in the Absence of Presynaptic Glutamate Release. Neuron *94*, 304–311.e4. https://doi.org/10.1016/j.neuron.2017.03.029.

24. Sando, R., Bushong, E., Zhu, Y., Huang, M., Considine, C., Phan, S., Ju, S., Uytiepo, M., Ellisman, M., and Maximov, A. (2017). Assembly of Excitatory Synapses in the Absence of Glutamatergic Neurotransmission. Neuron *94*, 312–321.e3. https://doi.org/10.1016/j.neuron.2017.03.047.

25. Imig, C., Min, S.W., Krinner, S., Arancillo, M., Rosenmund, C., Südhof, T.C., Rhee, J.S., Brose, N., and Cooper, B.H. (2014). The Morphological and Molecular Nature of Synaptic Vesicle Priming at Presynaptic Active Zones. Neuron *84*, 416–431. https://doi.org/10.1016/J.NEURON.2014.10.009.

26. Lu, W., Bushong, E.A., Shih, T.P., Ellisman, M.H., and Nicoll, R.A. (2013). The cell-autonomous role of excitatory synaptic transmission in the regulation of neuronal

structure and function. Neuron *78*, 433–439. https://doi.org/10.1016/J.NEURON.2013.02.030.

27. DeBello, W., and Zito, K. (2017). Within a Spine's Reach. In The Rewiring Brain (Elsevier), pp. 295–317. https://doi.org/10.1016/B978-0-12-803784-3.00014-7.

28. Hedrick, N.G., Lu, Z., Bushong, E., Singhi, S., Nguyen, P., Magaña, Y., Jilani, S., Lim, B.K., Ellisman, M., and Komiyama, T. (2022). Learning binds new inputs into functional synaptic clusters via spinogenesis. Nat. Neurosci. *25*, 726–737. https://doi.org/10.1038/s41593-022-01086-6.

29. Hwang, F.-J., Roth, R.H., Wu, Y.-W., Sun, Y., Kwon, D.K., Liu, Y., and Ding Correspondence, J.B. (2022). Motor learning selectively strengthens cortical and striatal synapses of motor engram neurons. Neuron *110*, 2790–2801.e5. https://doi.org/10.1016/j.neuron.2022.06.006.

30. Scholl, B., Thomas, C.I., Ryan, M.A., Kamasawa, N., and Fitzpatrick, D. (2021). Cortical response selectivity derives from strength in numbers of synapses. Nature *590*, 111–114. https://doi.org/10.1038/s41586-020-03044-3.

31. Chen, J.L., Villa, K.L., Cha, J.W., So, P.T.C., Kubota, Y., and Nedivi, E. (2012). Clustered Dynamics of Inhibitory Synapses and Dendritic Spines in the Adult Neocortex. Neuron *74*, 361–373. https://doi.org/10.1016/j.neuron.2012.02.030.

32. Nishiyama, J., and Yasuda, R. (2015). Biochemical Computation for Spine Structural Plasticity. Neuron *87*, 63–75. https://doi.org/10.1016/j.neuron.2015.05.043.

33. Harvey, C.D., Yasuda, R., Zhong, H., and Svoboda, K. (2008). The spread of Ras activity triggered by activation of a single dendritic spine. Science *321*, 136–140. https://doi.org/10.1126/SCIENCE.1159675/SUPPL_FILE/HARVEY.SOM.PDF.

34. Kumar, V., Zhang, M.X., Swank, M.W., Kunz, J., and Wu, G.Y. (2005). Regulation of Dendritic Morphogenesis by Ras–PI3K–Akt–mTOR and Ras–MAPK Signaling Pathways. J. Neurosci. *25*, 11288–11299. https://doi.org/10.1523/JNEUROSCI.2284-05.2005.

35. Azouz, R., Gray, C.M., Nowak, L.G., and McCormick, D.A. (1997). Physiological properties of inhibitory interneurons in cat striate cortex. Cereb. Cortex *7*, 534–545. https://doi.org/10.1093/CERCOR/7.6.534.

36. Guirado, R., Perez-Rando, M., Sanchez-Matarredona, D., Castillo-Gómez, E., Liberia, T., Rovira-Esteban, L., Varea, E., Crespo, C., Blasco-Ibáñez, J.M., and Nacher, J. (2014). The Dendritic Spines of Interneurons Are Dynamic Structures Influenced by PSA-NCAM Expression. Cereb. Cortex *24*, 3014–3024. https://doi.org/10.1093/CERCOR/BHT156.

37. Gulyás, A.I., Megías, M., Emri, Z., and Freund, T.F. (1999). Total Number and Ratio of Excitatory and Inhibitory Synapses Converging onto Single Interneurons of Different Types in the CA1 Area of the Rat Hippocampus. J. Neurosci. *19*, 10082–10097. https://doi.org/10.1523/JNEUROSCI.19-22-10082.1999.

38. Kawaguchi, Y., Karube, F., and Kubota, Y. (2006). Dendritic Branch Typing and Spine Expression Patterns in Cortical Nonpyramidal Cells. Cereb. Cortex *16*, 696–711. https://doi.org/10.1093/CERCOR/BHJ015.

39. Keck, T., Scheuss, V., Jacobsen, R.I., Wierenga, C.J., Eysel, U.T., Bonhoeffer, T.,

and Hübener, M. (2011). Loss of sensory input causes rapid structural changes of inhibitory neurons in adult mouse visual cortex. Neuron *71*, 869–882. https://doi.org/10.1016/j.neuron.2011.06.034.

40. Kubota, Y., Karube, F., Nomura, M., Gulledge, A.T., Mochizuki, A., Schertel, A., and Kawaguchi, Y. (2011). Conserved properties of dendritic trees in four cortical interneuron subtypes. Sci. Rep. *1*, 89. https://doi.org/10.1038/srep00089.

41. Perez-Rando, M., Castillo-Gómez, E., Guirado, R., Blasco-Ibañez, J.M., Crespo, C., Varea, E., and Nacher, J. (2017). NMDA Receptors Regulate the Structural Plasticity of Spines and Axonal Boutons in Hippocampal Interneurons. Front. Cell. Neurosci. *11*, 166. https://doi.org/10.3389/FNCEL.2017.00166.

42. Peters, A., and Regidor, J. (1981). A reassessment of the forms of nonpyramidal neurons in area 17 of cat visual cortex. J. Comp. Neurol. *203*, 685–716. https://doi.org/10.1002/CNE.902030408.

43. Sancho, L., and Bloodgood, B.L. (2018). Functional Distinctions between Spine and Dendritic Synapses Made onto Parvalbumin-Positive Interneurons in Mouse Cortex. Cell Rep. *24*, 2075–2087. https://doi.org/10.1016/j.celrep.2018.07.070.

44. Kim, J., Lee, S., Jung, K., Oh, W.C., Kim, N., Son, S., Jo, Y.J., Kwon, H.B., and Do Heo, W. (2019). Intensiometric biosensors visualize the activity of multiple small GTPases in vivo. Nat. Commun. *10*, 211. https://doi.org/10.1038/s41467-018-08217-3.

45. Ye, X., and Carew, T.J. (2010). Small G Protein Signaling in Neuronal Plasticity and Memory Formation: The Specific Role of Ras Family Proteins. Neuron *68*, 340–361. https://doi.org/10.1016/J.NEURON.2010.09.013.

46. Wang, X., Zhang, C., Szábo, G., and Sun, Q.Q. (2013). Distribution of CaMKIIα expression in the brain in vivo, studied by CaMKIIα-GFP mice. Brain Res. *1518*, 9–25. https://doi.org/10.1016/J.BRAINRES.2013.04.042.

47. Tjia, M., Yu, X., Jammu, L.S., Lu, J., and Zuo, Y. (2017). Pyramidal neurons in different cortical layers exhibit distinct dynamics and plasticity of apical dendritic spines. Front. Neural Circuits *11*, 43. https://doi.org/10.3389/FNCIR.2017.00043/ABSTRACT.

48. Eavri, R., Shepherd, J., Welsh, C.A., Flanders, G.H., Bear, M.F., and Nedivi, E. (2018). Interneuron simplification and loss of structural plasticity as markers of aging-related functional decline. J. Neurosci. *38*, 8421–8432. https://doi.org/10.1523/JNEUROSCI.0808-18.2018.

49. Hájos, N., Acsády, L., and Freund, T.F. (1996). Target Selectivity and Neurochemical Characteristics of VIP-immunoreactive Interneurons in the Rat Dentate Gyrus. Euro. J. Neurosci. *8*, 1415–1431. https://doi.org/10.1111/j.1460-9568.1996.tb01604.x.

50. Huntley, M.A., Srinivasan, K., Friedman, B.A., Wang, T.-M., Yee, A.X., Wang, Y., Kaminker, J.S., Sheng, M., Hansen, D.V., and Hanson, J.E. (2020). Genome-Wide Analysis of Differential Gene Expression and Splicing in Excitatory Neurons and Interneuron Subtypes. J. Neurosci. *40*, 958–973. https://doi.org/10.1523/JNEUROSCI.1615-19.2019.

51. Wu, M., Minkowicz, S., Dumrongprechachan, V., Hamilton, P., and Kozorovitskiy, Y. (2021). Ketamine Rapidly Enhances Glutamate-Evoked Dendritic Spinogenesis in Medial Prefrontal Cortex Through Dopaminergic Mechanisms. Biol. Psychiatry *89*, 1096–1105.

https://doi.org/10.1016/J.BIOPSYCH.2020.12.022.

52. Glasgow, S.D., McPhedrain, R., Madranges, J.F., Kennedy, T.E., and Ruthazer, E.S. (2019). Approaches and limitations in the investigation of synaptic transmission and plasticity. Front. Synaptic Neurosci. 11, 20. https://doi.org/10.3389/FNSYN.2019.00020/BIBTEX.

53. Shiraishi-Yamaguchi, Y., and Furuichi, T. (2007). The Homer family proteins. Genome Biol. 8, 206. https://doi.org/10.1186/GB-2007-8-2-206.

54. Tao-Cheng, J.H., Thein, S., Yang, Y., Reese, T.S., and Gallant, P.E. (2014). Homer is concentrated at the postsynaptic density and does not redistribute after acute synaptic stimulation. Neuroscience 266, 80–90. https://doi.org/10.1016/J.NEUROSCIENCE.2014.01.066.

55. Straub, C., and Sabatini, B.L. (2014). How to grow a synapse. Neuron 82, 256–257. https://doi.org/10.1016/j.neuron.2014.03.033.

56. Busetto, G., Higley, M.J., and Sabatini, B.L. (2008). Developmental presence and disappearance of postsynaptically silent synapses on dendritic spines of rat layer 2/3 pyramidal neurons. J. Physiol. 586, 1519–1527. https://doi.org/10.1113/JPHYSIOL.2007.149336.

57. Hanse, E., Seth, H., and Riebe, I. (2013). AMPA-silent synapses in brain development and pathology. Nat. Rev. Neurosci. 14, 839–850. https://doi.org/10.1038/NRN3642.

58. Arellano, J.I., Benavides-Piccione, R., DeFelipe, J., and Yuste, R. (2007). Ultrastructure of Dendritic Spines: Correlation Between Synaptic and Spine Morphologies. Front. Neurosci. 1, 131–143. https://doi.org/10.3389/NEURO.01.1.1.010.2007/BIBTEX.

59. Alvarez, V.A., and Sabatini, B.L. (2007). Anatomical and Physiological Plasticity of Dendritic Spines. Annu Rev Neurosci. 30, 79–97. https://doi.org/10.1146/annurev.neuro.30.051606.094222.

60. Bhatt, D.H., Zhang, S., and Gan, W.-B. (2009). Dendritic Spine Dynamics. Annu. Rev. Physiol. 71, 261–282. https://doi.org/10.1146/annurev.physiol.010908.163140.

61. Fiala, J.C., Feinberg, M., Popov, V., and Harris, K.M. (1998). Synaptogenesis Via Dendritic Filopodia in Developing Hippocampal Area CA1. J. Neurosci. 18, 8900–8911. https://doi.org/10.1523/JNEUROSCI.18-21-08900.1998.

62. Runge, K., Cardoso, C., and de Chevigny, A. (2020). Dendritic Spine Plasticity: Function and Mechanisms. Front. Synaptic Neurosci. 12, 36.

63. Woolfrey, K.M., and Srivastava, D.P. (2016). Control of Dendritic Spine Morphological and Functional Plasticity by Small GTPases. Neural Plast. 2016, 3025948. https://doi.org/10.1155/2016/3025948.

64. Penzes, P., and Rafalovich, I. (2012). Regulation of the actin cytoskeleton in dendritic spines. Adv. Exp. Med. Biol. 970, 81–95. https://doi.org/10.1007/978-3-7091-0932-8_4.

65. Murakoshi, H., and Yasuda, R. (2012). Postsynaptic signaling during plasticity of dendritic spines. Trends Neurosci. 35, 135–143. https://doi.org/10.1016/j.tins.2011.12.002.

66. Tyssowski, K.M., DeStefino, N.R., Cho, J.H., Dunn, C.J., Poston, R.G., Carty, C.E., Jones, R.D., Chang, S.M., Romeo, P., Wurzelmann, M.K., et al. (2018). Different Neuronal Activity Patterns Induce Different Gene Expression Programs. Neuron 98, 530–546.e11. https://doi.org/10.1016/J.NEURON.2018.04.001.

67. Noguchi, J., Hayama, T., Watanabe, S., Ucar, H., Yagishita, S., Takahashi, N., and Kasai, H. (2016). State-dependent diffusion of actin-depolymerizing factor/cofilin underlies the enlargement and shrinkage of dendritic spines. Sci. Rep. 6, 32897. https://doi.org/10.1038/srep32897.

68. Shirao, T., and González-Billault, C. (2013). Actin filaments and microtubules in dendritic spines. J. Neurochem. 126, 155–164. https://doi.org/10.1111/jnc.12313.

69. Biou, V., Brinkhaus, H., Malenka, R.C., and Matus, A. (2008). Interactions between drebrin and Ras regulate dendritic spine plasticity. Eur. J. Neurosci. 27, 2847–2859. https://doi.org/10.1111/J.1460-9568.2008.06269.X.

70. Manabe, T., Aiba, A., Yamada, A., Ichise, T., Sakagami, H., Kondo, H., and Katsuki, M. (2000). Regulation of Long-Term Potentiation by H-Ras through NMDA Receptor Phosphorylation. J. Neurosci. 20, 2504–2511. https://doi.org/10.1523/JNEUROSCI.20-07-02504.2000.

71. Qu, W., Jeong, A., Zhong, R., Thieschafer, J.S., Gram, A., and Li, L. (2023). Deletion of Small GTPase H-Ras Rescues Memory Deficits and Reduces Amyloid Plaque-Associated Dendritic Spine Loss in Transgenic Alzheimer's Mice. Mol. Neurobiol. 60, 495–511. https://doi.org/10.1007/S12035-022-03082-0/TABLES/1.

72. Transcriptomics Explorer: Allen Brain Atlas: Cell Types https://celltypes.brain-map.org/rnaseq/mouse_ctx-hpf_smart-seq?selectedVisualization=Heatmap&colorByFeature=Cell+Type&colorByFeatureValue=Gad1.

73. Passafaro, M., Nakagawa, T., Sala, C., and Sheng, M. (2003). Induction of dendritic spines by an extracellular domain of AMPA receptor subunit GluR2. Nature 424, 677–681. https://doi.org/10.1038/nature01781.

74. Arstikaitis, P., Gauthier-Campbell, C., Huang, K., El-Husseini, A., and Murphy, T.H. (2011). Proteins That Promote Filopodia Stability, but Not Number, Lead to More Axonal-Dendritic Contacts. PLoS One 6, e16998. https://doi.org/10.1371/JOURNAL.PONE.0016998.

75. Linke, R., Soriano, E., and Frotscher, M. (1994). Transient dendritic appendages on differentiating septohippocampal neurons are not the sites of synaptogenesis. Brain Res. Dev. Brain Res. 83, 67–78. https://doi.org/10.1016/0165-3806(94)90180-5.

76. Wong, R.O.L., Yamawaki, R.M., and Shatz, C.J. (1992). Synaptic Contacts and the Transient Dendritic Spines of Developing Retinal Ganglion Cells. Eur. J. Neurosci. 4, 1387–1397. https://doi.org/10.1111/J.1460-9568.1992.TB00184.X.

77. Chang, M., Lee, O.C., Bu, G., Oh, J., Yunn, N.O., Ryu, S.H., Kwon, H.B., Kolomeisky, A.B., Shim, S.H., Doh, J., et al. (2022). Formation of cellular close-ended tunneling nanotubes through mechanical deformation. Sci. Adv. 8, 3995. https://doi.org/10.1126/SCIADV.ABJ3995/SUPPL_FILE/SCIADV.ABJ3995_MOVIES_S1_TO_S9.ZIP.

78. Überall, F., Hellbert, K., Kampfer, S., Maly, K., Villunger, A., Spitaler, M., Mwanjewe, J., Baier-Bitterlich, G., Baier, G., and Grunicke, H.H. (1999). Evidence That Atypical Protein Kinase C- and Atypical Protein Kinase C-Participate in Ras-mediated Reorganization of the F-actin Cytoskeleton. J. Cell Biol. 144, 413–425.

79. Makrodouli, E., Oikonomou, E., Koc, M., Andera, L., Sasazuki, T., Shirasawa, S., and Pintzas, A. (2011). BRAF and RAS oncogenes regulate Rho GTPase pathways to mediate migration and invasion properties in human colon cancer cells: A comparative study. Mol. Cancer 10, 118. https://doi.org/10.1186/1476-4598-10-118/FIGURES/10.

80. Leondaritis, G., and Eickholt, B.J. (2015). Short Lives with Long-Lasting Effects: Filopodia Protrusions in Neuronal Branching Morphogenesis. PLoS Biol. 13, e1002241. https://doi.org/10.1371/JOURNAL.PBIO.1002241.

81. Rostami, J., Holmqvist, S., Lindström, V., Sigvardson, J., Westermark, G.T., Ingelsson, M., Bergström, J., Roybon, L., and Erlandsson, A. (2017). Human Astrocytes Transfer Aggregated Alpha-Synuclein via Tunneling Nanotubes. J. Neurosci. 37, 11835–11853. https://doi.org/10.1523/JNEUROSCI.0983-17.2017.

82. Wang, Y., Cui, J., Sun, X., and Zhang, Y. (2011). Tunneling-nanotube development in astrocytes depends on p53 activation. Cell Death Differ. 18, 732–742. https://doi.org/10.1038/cdd.2010.147.

83. Alarcon-Martinez, L., Villafranca-Baughman, D., Quintero, H., Kacerovsky, J.B., Dotigny, F., Murai, K.K., Prat, A., Drapeau, P., and Di Polo, A. (2020). Interpericyte tunnelling nanotubes regulate neurovascular coupling. Nature 585, 91–95. https://doi.org/10.1038/s41586-020-2589-x.

84. Scheiblich, H., Dansokho, C., Mercan, D., Schmidt, S.V., Bousset, L., Wischhof, L., Eikens, F., Odainic, A., Spitzer, J., Griep, A., et al. (2021). Microglia jointly degrade fibrillar alpha-synuclein cargo by distribution through tunneling nanotubes. Cell 184, 5089–5106.e21. https://doi.org/10.1016/J.CELL.2021.09.007.

85. Rustom, A., Saffrich, R., Markovic, I., Walther, P., and Gerdes, H.H. (2004). Nanotubular Highways for Intercellular Organelle Transport. Science 303, 1007–1010. https://doi.org/10.1126/SCIENCE.1093133/SUPPL_FILE/RUSTOM.SOM.PDF.

86. Rainy, N., Chetrit, D., Rouger, V., Vernitsky, H., Rechavi, O., Marguet, D., Goldstein, I., Ehrlich, M., and Kloog, Y. (2013). H-Ras transfers from B to T cells via tunneling nanotubes. Cell Death Dis. 4, e726. https://doi.org/10.1038/cddis.2013.245.

87. Ortin-Martinez, A., Yan, N.E., Tsai, E.L.S., Comanita, L., Gurdita, A., Tachibana, N., Liu, Z.C., Lu, S., Dolati, P., Pokrajac, N.T., et al. (2021). Photoreceptor nanotubes mediate the in vivo exchange of intracellular material. EMBO J. 40, e107264. https://doi.org/10.15252/EMBJ.2020107264/SUPPL_FILE/EMBJ2020107264-SUP-0016-MOVIEEV7.ZIP.

88. Tasaki, S., Xu, J., Avey, D.R., Johnson, L., Petyuk, V.A., Dawe, R.J., Bennett, D.A., Wang, Y., and Gaiteri, C. (2022). Inferring protein expression changes from mRNA in Alzheimer's dementia using deep neural networks. Nat. Commun. 13, 655. https://doi.org/10.1038/s41467-022-28280-1.

89. Moritz, C.P., Mühlhaus, T., Tenzer, S., Schulenborg, T., and Friauf, E. (2019). Poor transcript-protein correlation in the brain: negatively correlating gene products reveal neuronal polarity as a potential cause.

J. Neurochem. *149*, 582–604. https://doi.org/10.1111/JNC.14664.

90. Wei, Y.N., Hu, H.Y., Xie, G.C., Fu, N., Ning, Z.B., Zeng, R., and Khaitovich, P. (2015). Transcript and protein expression decoupling reveals RNA binding proteins and miRNAs as potential modulators of human aging. Genome Biol. *16*, 41. https://doi.org/10.1186/S13059-015-0608-2/FIGURES/5.

91. Kumar, P., Goettemoeller, A.M., Espinosa-Garcia, C., Tobin, B.R., Tfaily, A., Nelson, R.S., Natu, A., Dammer, E.B., Santiago, J.V., Malepati, S., et al. (2024). Native-state proteomics of Parvalbumin interneurons identifies unique molecular signatures and vulnerabilities to early Alzheimer's pathology. Nat. Commun. *15*, 2823. https://doi.org/10.1038/s41467-024-47028-7.

92. Unterauer, E.M., Boushehri, S.S., Jevdokimenko, K., Masullo, L.A., Ganji, M., Sograte-Idrissi, S., Kowalewski, R., Strauss, S., Reinhardt, S.C.M., Perovic, A., et al. (2024). Spatial proteomics in neurons at single-protein resolution. Cell *187*, 1785–1800.e16. https://doi.org/10.1016/J.CELL.2024.02.045.

93. Opitz-Araya, X., and Barria, A. (2011). Organotypic Hippocampal Slice Cultures. J. Vis. Exp. *3*, 2462. https://doi.org/10.3791/2462.

94. Woods, G., and Zito, K. (2008). Preparation of Gene Gun Bullets and Biolistic Transfection of Neurons in Slice Culture. J. Vis. Exp. *12*, 675. https://doi.org/10.3791/675.

95. Franklin, K.B.J., and Paxinos, G. (2019). Paxinos and Franklin's the Mouse Brain in Stereotaxic Coordinates.

96. Ferreira, J.S., Dupuis, J.P., Kellermayer, B., Bénac, N., Manso, C., Bouchet, D., Levet, F., Butler, C., Sibarita, J.B., and Groc, L. (2020). Distance-dependent regulation of NMDAR nanoscale organization along hippocampal neuron dendrites. Proc. Natl. Acad. Sci. USA *117*, 24526–24533. https://doi.org/10.1073/PNAS.1922477117/-/DCSUPPLEMENTAL.

STAR★METHODS

KEY RESOURCES TABLE

REAGENT or RESOURCE	SOURCE	IDENTIFIER
Antibodies		
Guinea pig anti-Bassoon antibody	Synaptic Systems	Cat# 141 004; RRID: AB_2290619
Mouse anti-Parvalbumin antibody	Swant	Cat#. 235; RRID: AB_10000343
Rabbit anti-Homer1 antibody	Synaptic Systems	Cat#. 160 003; RRID: AB_887730
Rabbit anti-H-Ras antibody	Proteintech	Cat#. 18295-1-AP; RRID: AB_2121046
Goat Anti-Guinea pig IgG H&L Alexa Fluor® 405	Abcam	Cat# ab175678; RRID: AB_2827755
Goat anti-Mouse IgG H + L Alexa Fluor™ 633	ThermoFisher	Cat# A-21052; RRID: AB_2535719
Goat anti-Rabbit IgG H + L Alexa Fluor™ 633	ThermoFisher	Cat# A-21071; RRID: AB_2535732
Bacterial and virus strains		
AAV-CAG-B3-RafRBD-2A-GA-HRas	This paper	Upon request
AAV-CAG-DIO-ddFPB-RafRBD-2A-ddGFPA-HRas	This paper	Upon request
AAV-CAG-DIO-ddFPB-RafRBD-2A-ddGFPA	This paper	Upon request
AAV-CAG-DIO-ddFPB-2A-ddGFPA	This paper	Upon request
AAV-CAG-tdTomato	Edward Boyden	RRID: Addgene_59462
AAV1-Camk2-0.4-Cre-SV40	James M. Wilson Lab	RRID: Addgene_105558
AAV9-CAG-Flex-tdTomato	Edward Boyden	RRID: Addgene_28306
Chemicals, peptides, and recombinant proteins		
Adenosine triphosphate (ATP)	Sigma-Aldrich	Cat# A2383-1G
Ascorbic Acid	Sigma-Aldrich	Cat# A92902
Bicuculine	Enzo	Cat# BML-EA149-005
Calcium chloride (CaCl)	Honeywell Fluka	Cat# 21114-1L
Cesium hydroxide	Sigma-Aldrich	Cat# 232041-50G
DAPI Fluoromount-G	SouthernBiotech	Cat# 0100-20
D-APV	Sigma-Aldrich	Cat# A528
D-Glucose	Sigma-Aldrich	Cat# G7021
EGTA	Sigma-Aldrich	Cat# E0396-10G
Gluconic acid	Sigma-Aldrich	Cat# G1951
Guanosine triphosphate (GTP)	Sigma-Aldrich	Cat# G8877-25MG
HEPES	Sigma-Aldrich	Cat# H3375
Horse serum	Thermo Fisher	Cat# 26050-088
Isoflurane	MWI	Cat# 07-890-8115
L-Glutamine	Thermo Fisher	Cat# 25030081
Lidocaine N-ethyl bromide	Sigma-Aldrich	Cat# L5783
Magnesium chloride (MgCl)	Honeywell Fluka	Cat# 63020-1L
Magnesium sulfate ($MgSO_4$)	Sigma-Aldrich	Cat# M3409-10X1ML
Meloxicam	Bio-Serv	Cat# MD275-0125
MEM Eagle medium	Thermo Fisher	Cat# 11965092
MNI glutamate	Tocris	Cat# 1490
Normal goat serum	Thermo Fisher	Cat# 50062Z
Paraformaldehyde (PFA)	Thermo Fisher	Cat# J19943.K2

(Continued on next page)

Continued

REAGENT or RESOURCE	SOURCE	IDENTIFIER
Phosphate-buffered saline (PBS)	Thermo Fisher	Cat.# 10010049
Phosphocreatine	Sigma-Aldrich	Cat# P7936-1G
Potassium chloride (KCl)	Sigma-Aldrich	Cat# 1603311000
Sodium bicarbonate (NaHCO$_3$)	Sigma-Aldrich	Cat# S6014
Sodium phosphate monobasic monohydrate (NaH$_2$PO$_4$)	Sigma-Aldrich	Cat# S5011
Sucrose	Sigma-Aldrich	Cat# S9378-1KG
TTX	Abcam	Cat# ab120055
Deposited data		
Allen Brain Transcriptomics Explorer	Allen Brain Institute	https://celltypes.brain-map.org/rnaseq/mouse_ctx-hpf_10x
Spine Morphology Analysis	This study	Zenodo DOI: 0000-0003-1168-5458
Transcriptomics of cortical excitatory and inhibitory neurons	Huntley et al.[50]	http://research-pub.gene.com/NeuronSubtypeTranscriptomes
Experimental models: Organisms/strains		
Wild type C57BL/6J	The Jackson Laboratory	Cat# 000664; RRID: IMSR_JAX:000664
PV-Cre: B6.129P2-Pvalb$^{tm1(cre)Arbr}$/J	The Jackson Laboratory	Cat# 017320; RRID: IMSR_JAX:017320
VIP-Cre: STOCK Vip$^{tm1(cre)Zjh}$/J	Hey-Kyoung Lee Lab	Cat# 010908; RRID: IMSR_JAX:010908
Software and algorithms		
FIJI (ImageJ)	NIH	https://fiji.sc/
Origin Lab	Origin Lab	http://www.originlab.com/index.aspx?go=Products/Origin/Statistics
Illustrator CS6	Adobe	http://www.adobe.com/products/illustrator.html
Imaris 9.9.1	Oxford Instruments	https://imaris.oxinst.com/packages
MATLAB	MathWorks	https://www.mathworks.com/products/matlab.html
Other		
Betadine solution	Purdue product LP	Cat# 19-061617
Cell culture inserts	Millipore	Cat# PICM0RG50
Gold particles	Bio-Rad	Cat# 1652264
Hair removal lotion	Nair	Cat# 22600223191
ProLong™ Glass Antifade Mountant	ThermoFisher	Cat# P36982
Systane Ophthalmic Ointment	Norvartis	Cat# B004RSQGWC
Vetbond tissue adhesive	3M Animal care products	Cat# 1469C

RESOURCE AVAILABILITY

Lead contact

Further information and request for resources, data or analysis code should be directed to and will be fulfilled by the Lead Contact, Hyung-Bae Kwon (hkwon29@jhmi.edu).

Materials availability

Plasmids generated in this study will be available from the lead contact upon request and are in the process to be deposited to Addgene.

Data and code availability

- Data: Microscopy and electrophysiology data reported in this paper will be shared by the lead contact upon request.

- Code: All original code has been deposited at Zenodo and is publicly available as of the date of publication. DOIs are listed in the key resources table.
- Any additional information required to reanalyze the data reported in this paper is available from the lead contact upon request.

EXPERIMENTAL MODEL AND SUBJECT DETAILS

Animals

C57BL/6 (4–9 weeks old), PV-Cre (4–9 weeks old) and VIP-Cre mice (4–9 weeks old) from Jackson laboratory (Bar Harbor, ME, USA) were used for experiments. All mice were maintained in a temperature and humidity-controlled facility following a 12 h light/12 h dark cycle with food and water available *ad libitum*. Control and test group animals were randomly chosen, and similar numbers of male and female mice were used for experiments. All experimental procedures were carried out in accordance with protocols (approval number: MO22M170) approved by the Johns Hopkins University Animal Care (email, ACUC@jhmi.edu) and Use Committee, the Max Planck Florida Institute for Neuroscience Institutional Animal Care and Use Committee (approved protocol number: 18-008), and the National Institutes of Health guidelines.

Tissue culture

Newborn C57BL/6 pups (1–2 days postnatally) were prepared for organotypic hippocampal slice cultures according to published procedure.[93] In short: Preparations were executed in an aseptic environment. Pups were decapitated, the brains were surgically removed and placed into ice-cold dissection medium (in mM: 1 $CaCl_2$, 5 $MgCl_2$, 10 D-Glucose, 4 KCl, 26 $NaHCO_3$, 234 Sucrose). Each hemisphere's cortices were isolated and transferred onto a tissue chopper stage in a sterile preparation hood. Any excess liquid around the tissue was removed before slicing the cortices into 300 μm thick coronal sections. For easier handling, slices were transferred to a plastic dish containing culture medium (in mM: 1 L-Glutamine, 1 $CaCl_2$, 2 $MgSO_4$, 13 D-Glucose, 5.3 $NaHCO_3$, 30 HEPES; 8.4 g/L MEM Eagle medium, 1 mg/L Insulin; 20% Horse serum, 0.00125% Ascorbic Acid) and then placed one-by-one onto small membrane cell culture inserts (Millipore, Burlington, MD). Maximally three cortical slices were cultured in each cell culture insert. Slices were maintained in culture medium for up to 2 weeks at 37°C/5% CO_2 changing 70% of the medium every 2–3 days. Slices were transfected 1 day after preparation using biolistic gene transfer as described previously.[94] A total of 10 μg of tdTomato alone or together with 30 μg pCAG-B3-RafRBD-2A-GA-HRas were coated onto 6–7 mg of gold particles. Slices were imaged 7–11 days after transfection.

METHODS DETAILS

Animal surgery and viral stereotaxic injection

Surgeries were conducted on ∼4-week-old mice in aseptic conditions using a small animal stereotactic setup (Kopf instruments, Tujunga, CA, USA). Mice were fully anesthetized in a closed chamber with isoflurane (5%) before moving animals to the stereotaxic setup where the isoflurane concentration was reduced to 2% and the mice's head was fixed. Ophthalmic ointment (Puralube Vet Ophthalmic Ointment) was applied to both eyes to prevent drying and body temperature (37 °C) was maintained by a thermostatically controlled heating pad (Harvard Apparatus, Holliston, MA, USA). To reduce the infection risk, mice's hair was removed with hair removal lotion (Nair, Church & Dwight) and the exposed scalp was subsequently disinfected three times alternately with 10% betadine solution (Purdue product LP, Stamford, CT, USA) and 70% ethanol wipes. A minor incision of the scalp was made, and the periosteum removed to allow for a small craniotomy (∼0.5 mm in diameter) over the injection site. To ensure the correct placement of the craniotomy lambda and bregma lines were used for orientation. The coordinates of the motor cortex for viral injection were anteroposterior (AP) +0.25 mm from bregma, mediolateral (ML) +/−1.5 mm from bregma, and dorsoventral (DV) −0.3 mm from the brain surface. The viral constructs (0.5 μl per hemisphere) were injected via a beveled glass micropipette (tip size 10–20 μm diameter, Braubrand), backfilled with mineral oil. Flow rate (150–250 nL/min) was regulated by a syringe pump (World Precision Instruments). The glass micropipette was fixed in place for 5 additional minutes after injection ended to minimize backflow. Finally, the scalp was stitched using vetbond glue (3M Animal care products, St. Paul, MN, USA). General analgesia (Buprenorphine SR, 0.6 mg/kg, or Meloxicam, 0125 mg) was injected subcutaneously or given orally, and mice were monitored until they recovered from anesthesia.

Preparation of acute cortical slices

Surgery animals recovered for 4 weeks after viral injection before they were anesthetized with isoflurane and either directly decapitated (for two-photon imaging) or cardiac perfused with ice-old cutting solution (in mM: 215 Sucrose, 20 D-Glucose, 26 $NaHCO_3$, 4 $MgSO_4$, 4 $MgCl$, 1.6 NaH_2PO_4, 1 $CaCl_2$, 2.5 KCl) prior to decapitation (for electrophysiology). The brains were quickly removed and submerged in ice-cold cutting solution. Cortical slices (300 μm thick) were prepared using a VT1000S vibrating microtome (Leica) and then incubated at 30°C for 30 min in a holding chamber filled with artificial cerebrospinal fluid (ACSF) (in mM: 124 NaCl, 3 KCl, 1.3 $MgSO_4$, 2.5 $CaCl_2$, 10 D-Glucose, 1.25 NaH_2PO_4, $NaHCO_3$). The holding chamber was moved to room temperature and the slices recovered for 30 more minutes before imaging or recording. All solutions were saturated for at least 30 min with 5% CO_2/95% O_2.

Two-photon imaging

Two-photon imaging was performed on transfected layer 2/3 pyramidal neurons from both organotypic and acute slices at either 10–14 days *in vitro* (DIV) or on postnatal days 58–62, respectively. Layer 2/3 VIP and PV interneurons were only studied in the acute slice imaging context. Slices were placed into a submersion-type chamber (Warner Instruments, Holliston, MA, USA) containing recirculating, oxygenated ACSF (in mM: 124 NaCl, 3 KCl, 1.3 $MgSO_4$, 2.5 $CaCl_2$, 10 D-Glucose, 1.25 NaH_2PO_4, $NaHCO_3$). Selected neurons were within 40 μm of the slice surface and image stacks (512 × 512 pixels; 0.049 μm/pixel) with 0.5 to 1-μm z-steps were collected from proximal apical (<50 μm from soma), distal apical (>50 μm from soma) and basal dendrites for pyramidal cells and from proximal (<50 μm from soma) and distal (>50 μm from soma) dendrites for VIP and PV interneurons using a two-photon microscope (Prairie Technologies, Inc) with a pulsed Tisapphire laser (MaiTai HP DeepSee, Spectra Physics) tuned to 920 nm (5–7.5 mW at the sample) under a 60× objective (1.0 NA, Olympus). For spine dynamics assessments in pyramidal cells, images of no more than 4 dendritic regions per neuron were taken every 10 min for a total of 1 h. All images shown are maximum projections of 3D image stacks after applying a median filter (2 × 2) to the raw image data.

Glutamate uncaging

Two-photon uncaging of MNI-glutamate was implemented, as previously described.[18] Two pulsed Ti:Sapphire lasers (Chameleon, Coherent, Santa Clara, CA) were used for imaging and uncaging with wavelengths of 920 nm and 720 nm, respectively. For MNI-glutamate uncaging on layer 2/3 pyramidal cells, 5 mM MNI-caged-glutamate was perfused into the slice chamber with existing, recirculating Mg^{2+}-free ACSF (in mM: 124 NaCl, 3 KCl, 0 $MgSO_4$, 2.5 $CaCl_2$, 10 D-Glucose, 1.25 NaH_2PO_4, $NaHCO_3$), and ~30 mW of 720 nm light at the back aperture of the objective (60× 1.0 NA objective, Olympus) was used to release the uncaging group. Glutamate high-frequency uncaging (HFU) stimuli consisted of 30 pulses (720 nm, 10–15 mW at the sample) with a duration of 4 ms delivered at 10 Hz. Uncaging locations were manually positioned in close vicinity (<0.5 μm) from the edge of the dendrite. The selected areas were well isolated with a smooth outer membrane and had at least one neighboring spine within 5 μm to ensure competency for spinogenesis. No more than four spinogenesis trials were performed from the same neuron. The mock stimulus was identical in parameters to the HFU stimulus, except carried out in the absence of caged compounds. Image stacks (512 × 512 pixels; 0.033 μm/pixel) with 1-μm z-steps were collected immediately before and after (<1 min) HFU as well as 2, 4, 6, 10 and 15 min after HFU to determine the time course of spine generation. If a new spine formed within the first 5 min after HFU, uncaging was denoted as success. Mock uncaging trials and observation of fluorescent changes of regions adjacent to uncaging spots were used as control.

Electrophysiology

Acute brain slices were transferred to a submersion-type, temperature-controlled recording chamber perfused with oxygenated ACSF (in mM: 124 NaCl, 3 KCl, 1.3 $MgSO_4$, 2.5 $CaCl_2$, 10 D-Glucose, 1.25 NaH_2PO_4, $NaHCO_3$) containing TTX (1 μM), D-APV (100 μM) and bicuculine (20 μM). Whole-cell recordings were performed at 30°C $\pm$ 2°C on visually identified and transfected layer 2/3 pyramidal neurons of the motor cortex using a MultiClamp 700B amplifier (Molecular Devices) and an upright microscope (E600 FN, Nikon) with oblique infrared and fluorescent illumination. Neurons were patched in voltage-clamp configuration (V_{hold} = −65 mV) using borosilicate glass pipettes (electrode resistances 3–7 MΩ) filled with internal solution (in mM: 120 CsOH, 120 Gluconic acid, 10 phosphocreatine, 0.5 GTP, 4 ATP, 8 KCl, 1 EGTA, 10 HEPES and 5 Lidocaine N-ethyl bromide). Data were acquired with a custom script in Igor Pro software (WaveMetrics). Trace duration was 10 s, and a test pulse was given at the beginning of each trace. Only traces with a stable steady-state holding current (<200 pA), a series resistance between 20 and 40 MΩ and an input resistance (R_i) > 150 MΩ were considered for further analysis. Additionally, if either the series or input resistance shifted by more than 15% from the average, the corresponding trace was excluded. Analysis of mEPSCs events was performed using a custom made MATLAB script (provided by Bryce Grier) and a minimum of 200 isolated events from each cell were quantified.

Immunohistochemistry and confocal imaging

On ∼ P55-P65, mice were deeply anesthetized with isoflurane and cardiac perfused with phosphate-buffered saline (PBS), followed by 4% paraformaldehyde (PFA). Brains were then collected and post-fixed in PFA for 24 h. Using a VT1000S vibratome (Leica Biosystems, Buffalo Grove, IL, USA) brains were coronally sectioned into 40 μm slices. Motor cortex sections were isolated using landmarks and neuroanatomical nomenclature in accordance with the mouse brain atlas.[95] Slices were then washed for 30 min with 50% ethanol, followed by a 1-h blocking step with 10% normal goat serum in PBS and 0.2% Triton X-100. Primary antibodies (Homer1, 1:500, #160 006, Synaptic systems; Bassoon, 1:300, # 141 004, Synaptic systems; H-Ras, 1:30, # 18295-1-AP, Proteintech; Parvalbumin, # 235, Swant, 1:500) were incubated on sections for 3 days at 4°C. Subsequently, sections were rinsed three times with PBS and incubated with species-appropriate secondary antibodies for 3 h (Goat anti-guinea pig IgG Alexa Fluor 405, Abcam, ab175678; Goat anti-rabbit IgG Alexa Fluor 633, Thermo Fisher Scientific, A-11036, Goat anti-mouse IgG Alexa Fluor 633, Thermo Fisher Scientific, A- 21050). After another round of three PBS washes, slices were mounted onto microscope slides (VWR, Atlanta, GA) using mounting product (ProLong Glass Antifade Mountant, ThermoFisher) and stored at a dark and dry place to polymerize for at least 24 h before imaging. Images of layer 2/3 pyramidal neurons in motor cortex were acquired using an upright laser scanning confocal microscope (Zeiss LSM800, Germany) with 2.5× or 63× oil objectives. To improve signal-to-noise ratios, images were deconvolved via a custom-made MATLAB script.

QUANTIFICATION AND STATISTICAL ANALYSIS

Structural imaging analysis

The individuals who performed the structural imaging analyses were blinded. Only dendritic segments, which fulfilled certain criteria, were selected for analysis. For each neuron the dendritic segments arose from the same cell body and their distance from it was traceable. Dendritic segments had to appear healthy, well-isolated, and protrusions were easily distinguishable from background signals. Moreover, a minimum of 5 dendritic segments per neuron were imaged and analyzed to allow for average protrusion density calculations. Spine numbers and morphology of two-photon images were determined using a custom-made MATLAB Script. In detail, the script was designed to enable semi-automated measurement of spine morphology from user input. The approximate locations of a spine head (point 1) and its origin where its neck protruded (point 2) were manually selected. Then the script marked the potential position of the spine head (point 1) to a pixel with the highest fluorescent intensity in the region of interest (r = 8 pixels from user input). To estimate real spine neck length, the distance between the spine head and dendrite was measured between two peaks of an intensity profile from a line connecting points 1 and 2. The thickness of the spine head was measured as the full-width half maximum (FWHM) from the intensity profile from a line (l = 30 pixels) which was perpendicular to the previous line connecting points 1 and 2, and centered on point 1. Next, to assess the total protrusion number of a neuron or different dendritic segments of a neuron (apical proximal, apical distal or basal) the sum of the detected protrusion was divided by the total dendrite length of each sector. Protrusions emanating from dendritic regions 0–50 μm away from the soma were counted as proximal for PV and VIP INs or apical proximal for PyNs, while any protrusions >50 μm from the soma were categorized as distal or apical distal, respectively. This Criterium was consistent with previous studies.[96] Protrusions were classified as filopodia if protrusion necks were longer than 3.5 μm and protrusion heads thinner than 0.45 μm. The rest were classified as spines. For protrusion dynamic analysis, timelapse images were carefully investigated marking protrusions which changed their appearance between timepoints manually. The ratio of newly formed or eliminated protrusions per dendrite per neuron was compared.

Immunohistochemistry image analysis

Imaris 9.9.1 was used to analyze and compare the antibody staining patterns of Homer1 and Bassoon between the H-Ras and ΔH-Ras (control) neurons, which were initially blinded. For each neuron imaged, 2–3 dendritic sections with clearly visible protrusions were cropped and used for analysis. Dendrite diameters and protrusions, shown by the red channel, were reconstructed manually using the filament tool. Dendrite length and protrusion number were recorded and protrusion densities calculated. Protrusions were then isolated as separate filaments and a new gray channel was created to represent them, which was then used to create protrusion surfaces. Next, Homer1 puncta, represented by the far-red channel, and the Bassoon puncta, represented by the blue channel, were reconstructed as surfaces. Homer1 within 0 μm of the spine surfaces and Bassoon within 0.1 μm of the spine surfaces (measurement taken from edge of one surface to edge of the other surface) were isolated as new surfaces. The number of protrusions with a Homer1 surface contact and the number of protrusions with a Bassoon surface contact were recorded.

Statistics

All statistical analyses were executed with Origin 2020b (OriginLab Corp., Northampton, MA). For datasets, where outliers were suspected, Grubb's tests were conducted and if datapoints were significant outliers they were excluded from the analysis. Before any further statistical analysis, the probability distributions of each dataset were compared using the Kolmogorov-Smirnov normality test for samples sizes >50 and the Shapiro Wilk normality test for sample sizes <50. Differences in variance were tested via the Levene test. Unless otherwise stated, parametric tests were carried out by t test, one-way ANOVA or two-way ANOVA followed by the Tukey post-hoc test if applicable for comparisons of interactions. Non-parametric data were analyzed by Kolmogorov-Smirnov test or Kruskal-Wallis one-way ANOVA followed by the Dunn post hoc analysis for comparisons of interactions. Cumulative frequency distributions were assessed via Kruskal-Wallis tests and subsequent Dunn post hoc analysis for comparison of interactions. Success rate of *de novo* spinogenesis was compared by two-sided Fisher's exact test. Exact statistical details of experiments are noted in the figure legends. p values <0.05 were considered statistically significant. Data are presented as mean $\pm$ SEM for parametric data and as median $\pm$ IQR for non-parametric data.